

Cooperative elliptic instability of a vortex pair

By T. LEWEKE[†] AND C. H. K. WILLIAMSON

Sibley School of Mechanical and Aerospace Engineering, Upson Hall,
Cornell University, Ithaca, NY 14853-7501, USA

(Received 6 February 1997 and in revised form 14 November 1997)

In this paper, we investigate the three-dimensional instability of a counter-rotating vortex pair to short waves, which are of the order of the vortex core size, and less than the inter-vortex spacing. Our experiments involve detailed visualizations and velocimetry to reveal the spatial structure of the instability for a vortex pair, which is generated underwater by two rotating plates. We discover, in this work, a symmetry-breaking phase relationship between the two vortices, which we show to be consistent with a kinematic matching condition for the disturbances evolving on each vortex. In this sense, the instabilities in each vortex evolve in a coupled, or ‘cooperative’, manner. Further results demonstrate that this instability is a manifestation of an elliptic instability of the vortex cores, which is here identified clearly for the first time in a real open flow. We establish a relationship between elliptic instability and other theoretical instability studies involving Kelvin modes. In particular, we note that the perturbation shape near the vortex centres is unaffected by the finite size of the cores. We find that the long-term evolution of the flow involves the inception of secondary transverse vortex pairs, which develop near the leading stagnation point of the pair. The interaction of these short-wavelength structures with the long-wavelength Crow instability is studied, and we observe significant modifications in the longevity of large vortical structures.

1. Introduction

The study of elementary vortex flows has received much attention over the last decade. One of the reasons is linked to the renewed interest in the dynamics of coherent structures, which are basic ingredients of many turbulent flows. Recent experimental (Cadot, Douady & Couder 1995) and numerical investigations (Vincent & Meneguzzi 1991; Kida 1993) have demonstrated the presence of organized structures in these flows in the form of thin vortices of different lengths, which contain most of the vorticity of the flow. In order to understand the importance of these structures and their effect on the global statistical properties of the flow, it is necessary to analyse their elementary dynamics in simple flows containing a single vortex or a small number of interacting vortices. A pair of counter-rotating parallel vortices, which is the object of this study, is one of the most basic examples of such flows. In addition to its fundamental interest, this particular flow also has a strong and quite direct link to engineering applications,

[†] Present address: Institut de Recherche sur les Phénomènes Hors Équilibre, CNRS/Universités Aix-Marseille I & II, 12 avenue Général Leclerc, F-13003 Marseille, France.

since similar structures are found in the wake of aircraft. The strong and long-lived vortices behind large aircraft can impose an important rolling moment on neighbouring aircraft, which is particularly dangerous during take-off and landing (a well-known wake hazard), and which today is the principal factor limiting airport capacities by imposing limits on the time between aircraft departures. Detailed knowledge about the dynamics of vortex pairs is therefore directly relevant in this context.

The first three-dimensional stability analysis of a vortex pair was performed by Crow (1970), who showed that such a pair is unstable to perturbations which are symmetric with respect to the plane separating the vortices and which have an axial wavelength of around eight vortex spacings. The mechanism of instability is linked to the fact that each vortex experiences the effect of a plane strain induced by the other vortex. It is known from Kelvin (1880) that a sinusoidal displacement disturbance (bending wave) of a straight vortex filament rotates without change of shape around the vortex. In the presence of an external strain field (for example, due to the presence of a second vortex), this self-induced rotation can be diminished or augmented by the azimuthal velocity component of the strain field. When these two rotational components balance each other, the radial component of the strain field leads to exponential growth of the disturbance. The most unstable bending modes are those for which the self-induced rotation is small or zero.

Crow also identified two other bending-wave modes of instability, symmetric and antisymmetric, with a much shorter wavelength of around one vortex spacing. However, Widnall, Bliss & Tsai (1974) pointed out that these modes are spurious, since the expression used by Crow for the self-induced rotation is asymptotically valid for long waves only. It suggests a vanishing rotation rate for short waves, whereas the exact results from Kelvin's (1880) dispersion relation for perturbations of a vortex of finite core size show that this rotation rate continues to increase as the perturbation wavelength is decreased, which does not admit an instability for this type of bending-wave perturbation. Widnall *et al.* (1974) recalled, however, that other more complicated disturbance modes, associated with different branches of Kelvin's dispersion relation, do indeed have vanishing rotation rates for certain short wavelengths, and suggested that these modes are likely to lead to instability. This result from a qualitative argument was later confirmed by more rigorous stability analyses of a vortex filament in an externally imposed strain field (Moore & Saffman 1975; Tsai & Widnall 1976; Robinson & Saffman 1984).

Another more recent body of theoretical work, which relates directly to short-wave instabilities in vortical flows, considers the so-called 'elliptic instability'. Pierrhumbert (1986) and Bayly (1986) were the first to show that two-dimensional flows with elliptical streamlines are unstable with respect to three-dimensional disturbances. They found that there is no low-wavelength cut-off for the band of unstable perturbations, in the case of inviscid flow. Such a cut-off exists, however, for non-vanishing viscosity, as shown by Landman & Saffman (1987). Ideally these flows arise from a combination of constant vorticity and constant strain in an unbounded domain, but similar flows can be found locally in a great variety of situations, from transitional shear flows to fully developed turbulence. The mechanism of instability is linked to the periodic straining experienced by plane-wave disturbances that are advected by the rotating base flow, and which can lead to a resonant amplification if the wave and straining frequencies match. Waleffe (1990) showed that combinations of most unstable plane waves can lead to localized disturbances, which can satisfy certain (inviscid) boundary conditions, e.g. for flow in cylindrical containers with slightly elliptical cross-sections.

This also demonstrates that the same mechanism may still be responsible for instability in bounded elliptical flows in general, such as the strained vortices of finite core size, which are studied in this paper.

An alternative to classical tools of hydrodynamic instability theory has recently been introduced to fluid dynamics by Lifschitz and co-workers (Lifschitz & Hameiri 1991; Lifschitz 1994; Bayly, Holm & Lifschitz 1996), and is termed the ‘geometric optics’ stability theory. This theory is a powerful tool which provides local stability criteria based on the geometrical properties of the basic flows. It is found that, in an inertial frame, any steady inviscid flow with a stagnation point flow is linearly and nonlinearly unstable to short-wave perturbations (except in the neighbourhood of circular streamlines). In particular, it was demonstrated in these studies that the local regions around an elliptic flow stagnation point are unstable in a manner which is strongly related to the theory of unbounded elliptic flow. Extensions of the criteria found by Lifschitz and others, to the case where there is a background rotating flow, have been made by Leblanc & Cambon (1997, 1998).

Experimental results concerning the short-wavelength instability of vortex pairs, or of strained vortices in general, are very rare. Short waves were observed on vortex rings, first by Krutzsch (1939) and more recently by Maxworthy (1972), Widnall & Sullivan (1973) and Didden (1977); this phenomenon triggered the analysis of Widnall *et al.* (1974) on this problem. Locke, Hirska & Rubin (1993) describe the experimental observation of a short-wave instability on an artificially perturbed pair of straight vortices, resulting in an array of perpendicular secondary vortices. Thomas & Auerbach (1994) showed the existence of short waves on one vortex of a non-symmetric pair generated by starting and stopping the rotation of a single flat plate. Their visualizations showed that the perturbations on one of their vortices had a qualitative resemblance with the Kelvin mode proposed by Widnall *et al.* (1974) as a candidate for short-wavelength instability. These observations (as well as the ones on vortex rings in earlier studies) show similarities with some of the present visualization results and indicate that the same mechanism as the one analysed here was acting in those flows. A comparison with Widnall *et al.*'s (1974) theory, however, concerning the instability wavelength showed little agreement, which may partly be due to the lack of precise quantitative information about the base flow and the perturbations. In a very recent experimental and numerical study, Delisi & Robins (1997) have observed a small-scale instability of a vortex pair generated in a stratified fluid. Similarly, very few experimental results on elliptic instability exist in the literature. The published results of, for example, Vladimirov, Makarenko & Tarasov (1987) and Malkus (1989), are all concerned with flow inside a closed container and, although showing qualitative agreement with theory, they are mostly of a preliminary nature.

In the present study, we investigate the unforced short-wavelength instability of a symmetric counter-rotating vortex pair, which is the simplest example of a strained and bounded vortex configuration in an open flow. We show a photograph of such a vortex pair in cross-section in figure 1, prior to the onset of small-scale instability. After a description of the experimental apparatus and methods in § 2, we show in § 3 the overall features and symmetries of the instability. In § 4 we proceed with a detailed analysis of the observed disturbance flow field, and use qualitative and quantitative comparisons with the different theories on short-wave instabilities (Tsai & Widnall 1976; Waleffe 1990). We also show that these theories are compatible with each other and actually describe the same phenomenon. The late stages of the instability, which are specific to the vortex-pair base flow, and the effect of the short waves on the evolution of the large-scale features of the pair, are presented in § 5. The conclusions follow in § 6.

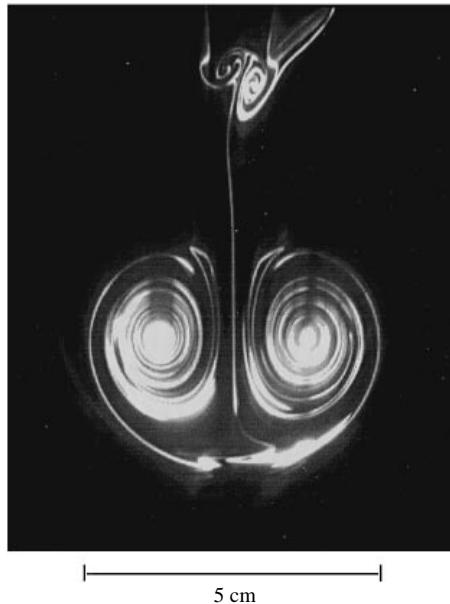


FIGURE 1. Fluorescent dye visualization of a symmetric counter-rotating vortex pair, seen in a plane perpendicular to the vortex axes shortly after the end of the plate motion.

2. Experimental details

The flow was studied in a rectangular water container with glass walls, measuring $180 \times 45 \times 60 \text{ cm}^3$. Horizontal vortex pairs were created near the water surface using a vortex generator shown schematically in figure 2(a). It consists of two flat aluminium plates, hinged on the upper side to a common base, and whose free edges were sharpened to an angle of 30° . The plates were anodized in black for protection against oxidation and good contrast for flow visualization. They could be moved in a symmetric way by a computer-controlled step motor located outside the water and linked to the plates by a system of gears and joints. When the flaps are impulsively closed from an initially almost vertical position, a pair of starting vortices (as shown in figure 1) is created at the sharp edges, which then continues to move down towards the bottom of the tank.

The vortex pair generator has a length of 170 cm, spanning almost the entire length of the tank. This high aspect ratio is necessary in order to minimize the influence of end effects that propagated into the central part of the flow. In a preliminary study, different end conditions were tested. With open ends, the vortex strength decreased towards the ends of the plates, since fluid was pushed out the sides instead of downwards. Large end plates touching the flaps induced a very strong axial flow in the cores of the starting vortices (tornado effect), spreading across their entire length well before the instabilities of interest developed. The end conditions finally adopted consist of two end plates extending downwards only to the tip of the plates. This leads to a 'short-circuiting' of the counter-rotating vortices at the ends and a successive formation of ring vortices in a chain reaction propagating into the remaining part of the pair. Only about one half of the initial vortex length remains unaffected by these end perturbations by the time the vortices reach the tank bottom. Much care was taken to guarantee the uniformity and precise alignment of the plate edges over

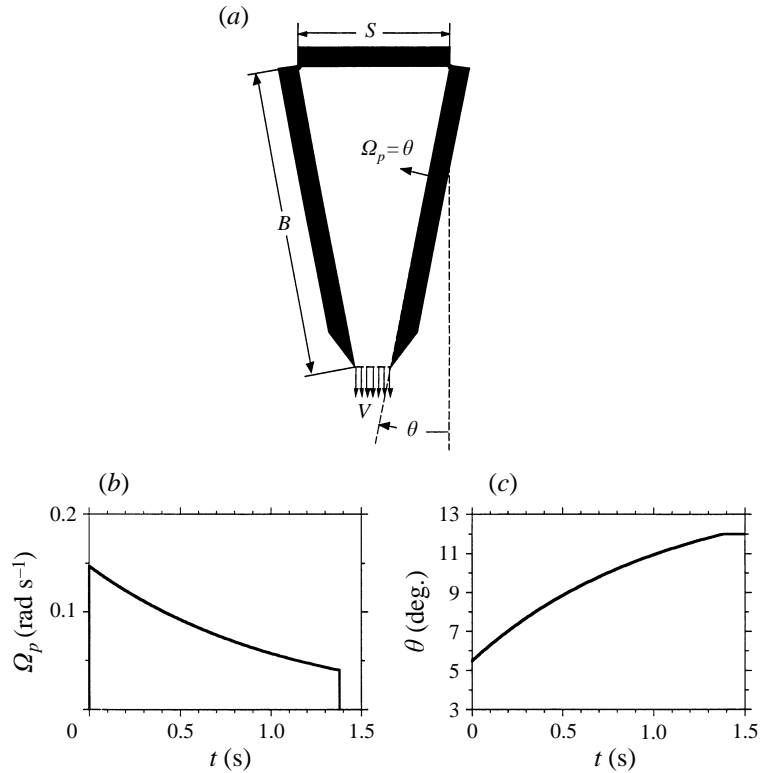


FIGURE 2. Vortex pair generator. (a) Schematic of the geometry, $S = 5.2$ cm, $B = 10.3$ cm. (b) and (c) Angular velocity and position of the plates as function of time. This motion profile leads to a constant mean outflow velocity V .

the entire length, as well as the overall symmetry of the set-up and the plate motion, since the flow proved to be extremely sensitive to these conditions.

The motion history of the plates used to study the short-wavelength instability is shown in figures 2(b) and 2(c). The angular velocity $\Omega_p = \dot{\theta}$ was varied in a way such that the mean outflow velocity $V = B\omega_p/(S/B - 2 \sin \theta)$ was constant during the time of motion of the plates. The expression for V is found by equating the volume swept per unit time by the two plates to the instantaneous gap size (between the plate tips), through which all the fluid is pushed, times the mean outflow velocity V . The motion was stopped before the edges were touching at $\theta = 14.5^\circ$ to avoid the final strong jet out of the vanishing gap, which could not easily be controlled. By the time the plate motion ended, the pair had moved down a distance of about 1.5 vortex separations, which was far enough to be unaffected by the very small counter-rotating stopping vortices (see figure 1).

In order to visualize the flow, fluorescent dye was placed inside the cavity between the plates, and illuminated with light from a 5 W Argon laser. Images were recorded on standard video tape using a high-resolution CCD shutter camera, or on 35 mm colour film.

Quantitative measurements of velocity fields were obtained by digital particle image velocimetry (DPIV). For this method, the flow was seeded with small plastic particles (microspheres from Bangs Laboratories Inc.) of mean diameter $75 \mu\text{m}$ and density 1.03 g cm^{-3} , illuminated by a sheet of laser light of 3–5 mm thickness. Although

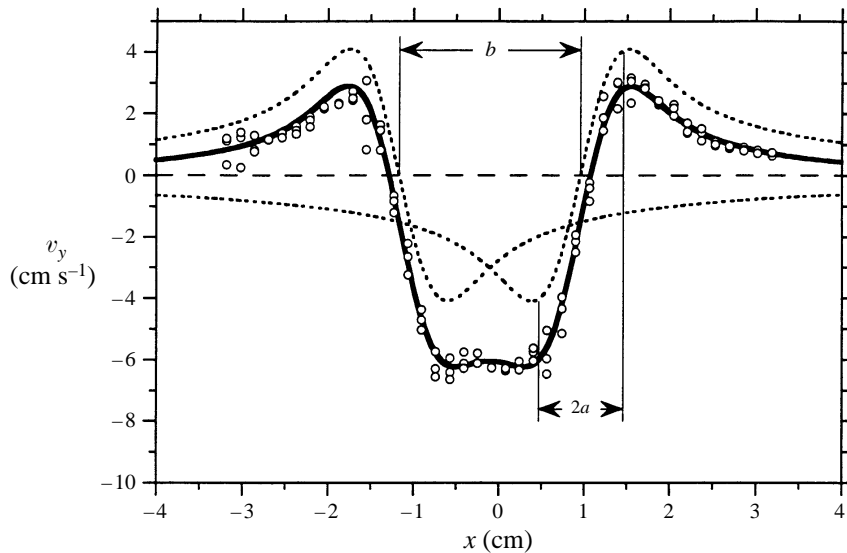


FIGURE 3. Profile of the vertical (azimuthal) velocity component on a line going through both vortex centres. A superposition of two Oseen vortices (dotted lines, equation (2.1)) is a good representation of the measured data. Least-squares fits allow the determination of the circulation Γ , the vortex spacing b , and the core size parameter a .

these relatively large particles may conceivably have an influence on the dynamics of turbulent flows (Elgobashi 1994), they can be expected to have a negligible effect on the present laminar vortex pair flows, since the smallest characteristic length scales are of the order of the vortex core size, i.e. more than two orders of magnitude larger than the particle diameter. In order to obtain a uniform particle distribution, the tank was stirred before each experiment. Measurements were made after waiting approximately 30 minutes for the fluid motion to die out. The time that the particles needed to settle down (drift velocity less than 0.05 mm s^{-1}) was far longer than this, so that a sufficient time interval was available for the measurements. Sequences of grey-scale images of the time-dependent flow were recorded on standard VHS video, again using a CCD camera. Fluid velocities were calculated from particle displacements obtained by two-step cross-correlations (with window shifting) between successive half-frames ($1/60 \text{ s}$ separation) of a single video image. The technique is an improved version of an algorithm by Guezennec & Kiritsis (1995), incorporating additional standard routines for the detection of spurious vectors and averaging described by Willert & Gharib (1994) and Westerweel (1994). The following is a list of typical DPIV parameters used in this study: image size: 624×476 pixels ($6 \times 4 \text{ cm}^2$ viewing area approximately); interrogation windows: 64×64 pixels (first correlation), 32×32 pixels (second correlation), in the half-images this corresponds to $6 \times 12 \text{ mm}^2$ and $3 \times 6 \text{ mm}^2$ regions respectively; window overlap: 50 %; image density: approximately 12 image pairs per interrogation window (second run); volume fraction of tracer particles: approximately 3×10^{-5} ; number of vectors: 20×15 (first correlation), 40×30 (second correlation); average number of spurious vectors: 6.

The DPIV analyses were performed on a 486 PC equipped with a Dipix image processing board. Two-dimensional vorticity fields were calculated from the velocities using the circulation method described e.g. by Abrahamson & Lonnes (1995). The

spatial resolution of the calculated vorticity distributions is of the order of the size of the contours (see figure 10 *a*).

DPIV was used to determine the initial conditions of the flow, which, for the present problem means the (two-dimensional) velocity field of the fully rolled-up vortices after the end of the plate motion. Precise knowledge of these conditions is essential for a meaningful comparison with theoretical results. A two-dimensional vortex pair can be characterized by the circulation Γ of each vortex and the separation b between the vortex centres. In addition, the internal structure can be described by a characteristic core size a , which is the radius of the tube around the vortex centre containing most of the vorticity (defined more precisely below). Figure 3 shows a profile of the vertical velocity component on a horizontal line going through both vortex centres (see figure 1), taken from measurements of the flow field shortly after the stopping of the plate motion. The bold-line fit shows that this profile can be approximated remarkably well by the one resulting from a superposition of two Oseen (or Lamb–Oseen) vortices, i.e. axisymmetric two-dimensional vortices with a Gaussian vorticity distribution, for which the azimuthal velocity v_ϕ ($= v_y$ for the special case in figure 3) as function of the distance r from the vortex centre is given by

$$v_\phi(r) = \frac{\Gamma}{2\pi r} \left[1 - \exp\left(-\frac{r^2}{a^2}\right) \right]. \quad (2.1)$$

Equation (2.1) describes a vortex with solid-body rotation close to the centre, potential flow far from the centre, and a smooth transition between the two regions. The parameter a is linked to the location r_{max} of maximum circumferential velocity by $r_{max} = 1.12a$. Fits like the one in figure 3 allow a determination of the vortex pair parameters $\{\Gamma, a, b\}$ by the use of a least-squares error method. The core size a increases with time t (measured from the start of the plate motion) due to the viscous diffusion of vorticity. For a two-dimensional Oseen vortex, $a = [4\nu(t - t_i)]^{1/2}$, where ν is the kinematic viscosity of the fluid. In the present set of experiments the virtual origin of vortex evolution was typically found to be $t_i \approx -2$ s, whereas the short-wave perturbation became visible around $t = 7$ s. At that time the core size a would vary only a few percent during the characteristic time of growth of the instability (see §4.5). Time is non-dimensionalized by

$$t = t^* \frac{2\pi b^2}{\Gamma}. \quad (2.2)$$

The second term on the right-hand side is the time it takes the pair, moving with a self-induced velocity $\Gamma/2\pi b$, to travel one vortex separation b . It is also the inverse of the strain induced by one vortex at the location of the centre of the other vortex, in the absence of this other vortex. We shall see, in §4, that the second vortex is deformed by the strain, and that the actual strain in the centre of each vortex is higher than the value $\Gamma/2\pi b^2$ in (2.1). The Reynolds number is based on the vortex circulation, $Re = \Gamma/\nu$, and has a range between 2400 and 2800 in this study. A typical vortex spacing is $b = 2.5$ cm, resulting in an initial aspect ratio (length/separation) of the pair of about 70. The initial core radius was close to one fifth of the vortex spacing: $a/b \approx 0.2$.

It is necessary, at this point, to briefly discuss the order of magnitude of errors of the numerical quantities presented in this paper. Certain length measurements, such as b , λ , d_{inv} , are measured optically from photographic images, and presented in §4.3 and §4.5. (As will be seen later, λ is the wavelength of perturbation, and d_{inv} the transverse length scale of the perturbation size.) For this purpose, we were careful to enlarge

the photographs, and to utilize a highly accurate electronic digitizing tablet. The relevant parameters in this paper have errors estimated as follows: $\Delta(\lambda/b) \approx \pm 3\%$; $\Delta(\lambda/d_{inv}) \approx \pm 5\%$. Other length measurements $\{a, b\}$ were evaluated from the Oseen representation of the vortices, as described above, yielding errors (based on scatter from one run to the next) $\Delta a \approx \pm 3\%$, $\Delta b \approx \pm 1\%$.

The measurement of vortex circulation Γ is made from the Oseen vortex fit, mentioned above, which may be compared with classical contour integrations around each vortex, using DPIV velocity distributions. We find the uncertainty in Γ , over a number of runs, to be $\Delta\Gamma \approx \pm 6\%$. The calculation of vorticity fields (ω) is clearly more prone to errors associated with the data analysis, in general reducing the peak values of computed ω , as the level of smoothing increases. We stress that our motivation with the vorticity contour plots is to present the qualitative vorticity distributions, rather than precise numerical values, in this case.

In order to determine the instability growth rate (in §4.5), we measure the amplitude of displacement of the vortex centreline (r_c), again from enlarged images, as for other length scales mentioned above. An estimate of the error in the determination of (r_c/λ) needs to take into account the fact that each resultant data point is actually the average of a large number (typically 16) of individual length measurements, rather than simply a single measurement, giving a computed error $\Delta(r_c/\lambda) \approx \pm 4\%$. This results in a computed uncertainty for the dimensional growth rate σ of $\pm 5\%$.

3. Cooperative short-wavelength interaction

In this section the overall qualitative features of the short-wavelength instability of a vortex pair are presented, mostly using results from flow visualization. We show, in figure 4, visualizations of different stages of the vortex pair evolution, at a Reynolds number $Re = 2750$. The descending pair is seen through the glass bottom of the tank in ‘front view’, i.e. it is moving towards the observer. The photograph in figure 4(a) was taken immediately after the end of the plate motion. The vortices are straight and uniform along their axes. Owing to the impulsive start of the plate motion, the centreline of each vortex is marked by a particularly bright filament of dye. In figure 4(b) two distinct instabilities have started to deform the pair, as follows. The symmetric large-scale deformation, which has an axial wavelength of about $6b$, is due to the Crow instability mentioned in §1. Recent experimental results concerning this long-wavelength vortex pair instability can be found in Leweke & Williamson (1998a). Simultaneously, another perturbation with a much smaller wavelength $\lambda < b$ is growing. It must be emphasized that this second disturbance is not simply a wavy displacement of the vortex without change in the cross-sectional structure, as for the Crow instability. Figure 4 shows that the short-wave instability modifies the internal structure of the vortex cores. The precise nature of this deformation will be considered in more detail in §4, but it is already visible in figure 4(b) that the inner and outer layers of each vortex are displaced in opposite radial directions.

The axial wavelength λ of the short waves was found to be close to 80% of the initial vortex spacing b . For comparison, Thomas & Auerbach (1994), who studied vortex pairs with similar geometric features, measured wavelengths in the range $0.6 < \lambda/b < 0.8$. However, we shall see in §4 that this wavelength scales on the core size a , which was not measured by Thomas & Auerbach (1994), rather than the vortex separation. Therefore the comparison between these two results can only be made with reservation.

The amplitude of the perturbation can be inferred from the deformation of the

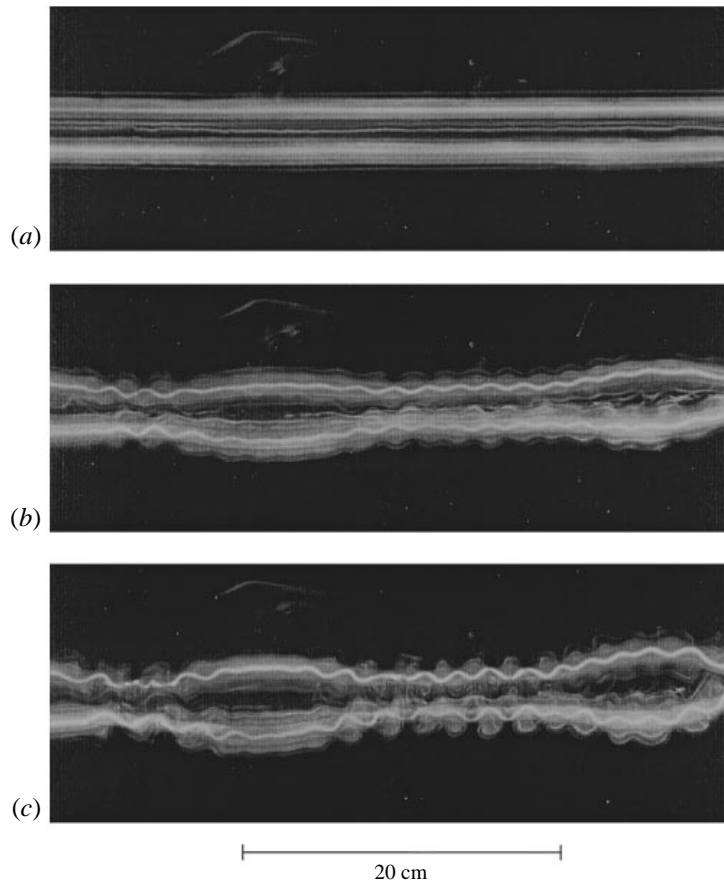


FIGURE 4. Visualization of vortex pair evolution under the combined action of long-wavelength (Crow) and short-wavelength instabilities. $Re = 2750$. The pair is moving towards the observer. (a) $t^* = 1.7$, (b) $t^* = 5.6$, (c) $t^* = 6.8$.

dye filament marking the vortex centre. It is interesting to note that the amplitude is larger in the regions where the large-scale instability brings the two vortices closer together. The instability growth rate can be expected to scale on the strain imposed on each vortex (see next section), and the mutually induced strain in a pair of vortices increases as the separation is decreased. Not surprisingly, it is in these regions of increased strain that the organized short-wave disturbance first starts to break down (figure 4c). This involves the inception of small perpendicular secondary vortex pairs in the vicinity of the leading stagnation point of the pair (see also figure 5a). Their interaction with the primary pair subsequently leads to a rapid decay of the large vortical structures. Details about the break-up and the late evolution of the flow are given in § 5.

An interesting and unexpected observation relates to the phase relationship between the short-wave perturbations on the two vortices. In the front views of figure 4, the vortex centres are, at each axial position, displaced in the same direction. This means that the initial reflectional symmetry of the flow, with respect to the plane separating the vortices, is lost. More detailed information about the orientation of the perturbations and their phase relationship can be obtained from figure 5. Figure 5(a)

shows a close-up of the central part of figure 4(c), and figure 5(b) the same flow seen simultaneously from the side. In the latter case, the displacements of the two vortex centres are clearly out of phase. This behaviour was observed systematically; it is not a random coincidence, and we should reiterate that the flow has not been forced in any manner. The instabilities on the two vortices are therefore found to evolve in a coupled, or ‘cooperative’, fashion.

In order to complete the picture of the three-dimensional orientation of the disturbance, a third perpendicular view along the primary vortex axes is needed. Since this was not accessible simultaneously in the experiments due to the arrangement of the laser optics, it was constructed digitally from the two other views. From each view in figure 5, the two vortex centres were seized as two-dimensional lines (using a digitizing tablet), as shown in figure 6. By identifying two corresponding points in the two views, the lines can be correlated to give three-dimensional curves representing the vortex centres. Figure 6(c) shows the projection of these curves on a plane perpendicular to the primary vortex axes, which corresponds to the missing end view of the pair. The centrelines are displaced in planes inclined by approximately 45° with respect to the horizontal. The orientation of these planes coincides with the directions of maximum stretching associated with the strain fields that the vortices induce on each other. This is already an indication that the short-wavelength instability is a direct consequence of this strain, in a way similar to the mechanism anticipated by Widnall *et al.* (1974). In this respect, it should also be emphasized that the perturbation does not rotate around the vortex axis: its structure is stationary while its amplitude keeps growing.

4. Elliptic instability of antisymmetric form

In this section we demonstrate that the short-wave instability we observe in a counter-rotating vortex pair is caused by an elliptic instability of the vortex cores. Based on theoretical studies treating this phenomenon, we make predictions for experimental observations and compare them to further results from flow visualizations and velocity measurements.

4.1. Theoretical background

We follow the treatment of Landman & Saffman (1987) and Waleffe (1990) and consider the stability of a two-dimensional base flow \mathbf{U} , which is a superposition of solid-body rotation (around the z -axis) and a potential stagnation-point flow (with stretching in the -45° direction) in an unbounded domain:

$$\mathbf{U} = \begin{pmatrix} 0 & -\frac{1}{2}\omega - \varepsilon & 0 \\ \frac{1}{2}\omega - \varepsilon & 0 & 0 \\ 0 & 0 & 0 \end{pmatrix} \begin{pmatrix} x \\ y \\ z \end{pmatrix}, \quad (4.1)$$

where ω and ε are the uniform vorticity and uniform strain rate, respectively, and Cartesian coordinates $x = (x, y, z)$ have been used. This flow is an exact solution of the Navier–Stokes equations, and its streamlines are ellipses with aspect ratio $E = [(\omega/2 + \varepsilon)/(\omega/2 - \varepsilon)]^{1/2}$. The solutions of the equations for the perturbations \mathbf{u} of this flow can be written in the form of Fourier modes

$$\mathbf{u} = \mathbf{v}(t) \exp [i\mathbf{k}(t)\mathbf{x}], \quad (4.2)$$

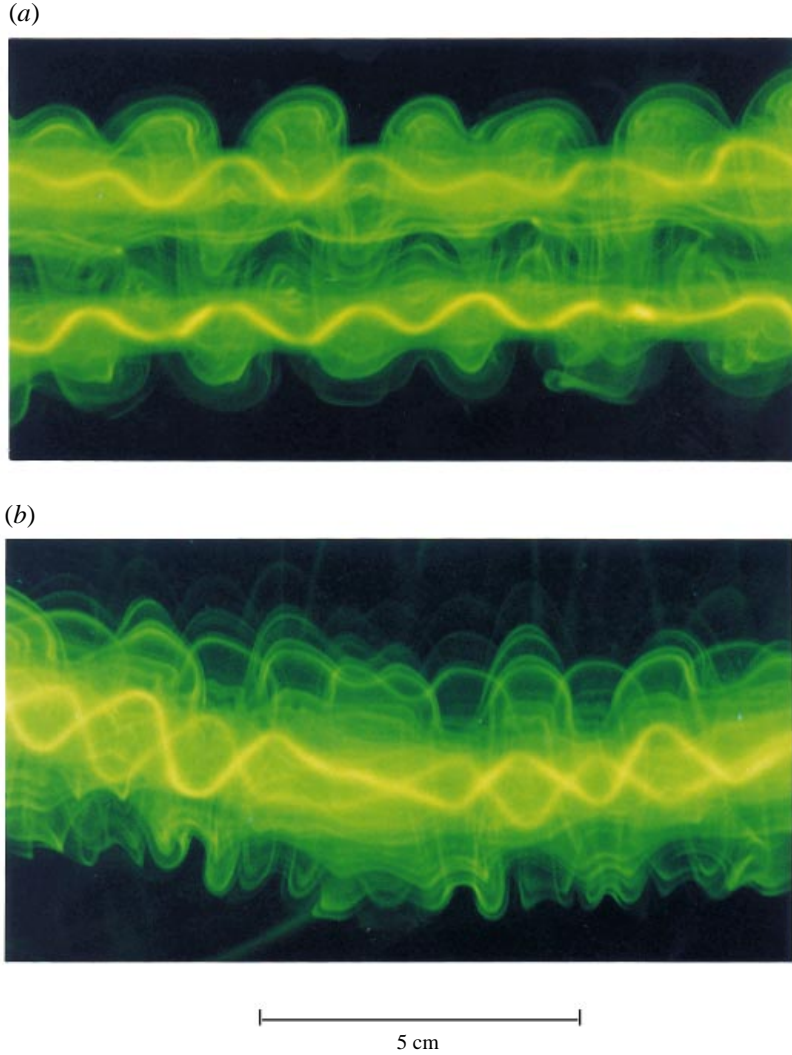


FIGURE 5. Simultaneous close-up views of the short-wavelength vortex pair perturbation in figure 4(c) from two perpendicular directions. $Re = 2750$, $t^* = 6.8$. (a) Front view (pair moving towards observer), (b) side view (pair moving down). The phase relation between the two vortices is clearly visible.

where the amplitude v and wave vector \mathbf{k} are both functions of time. The wave vector has the form

$$\mathbf{k} = k_o \left\{ \sin \theta \cos \left[\left(\frac{1}{4} \omega^2 - \varepsilon^2 \right)^{1/2} (t - t_o) \right], E \sin \theta \sin \left[\left(\frac{1}{4} \omega^2 - \varepsilon^2 \right)^{1/2} (t - t_o) \right], \cos \theta \right\}. \quad (4.3)$$

It precesses elliptically with frequency $(\omega^2/4 - \varepsilon^2)^{1/2}$ and (minimum) inclination θ with respect to the z -axis. The scale k_o is arbitrary in an unbounded domain. It is found that, for any non-zero strain, there exists a band of unstable wave vector angles θ leading to an exponentially growing perturbation amplitude v , i.e. to instability. We will see below (§4.5) that, for the vortex pairs in our study, the strain in the cores is approximately given by $\varepsilon = \Gamma / \pi b^2$. With $a/b \approx 0.2$, we see that this is small compared

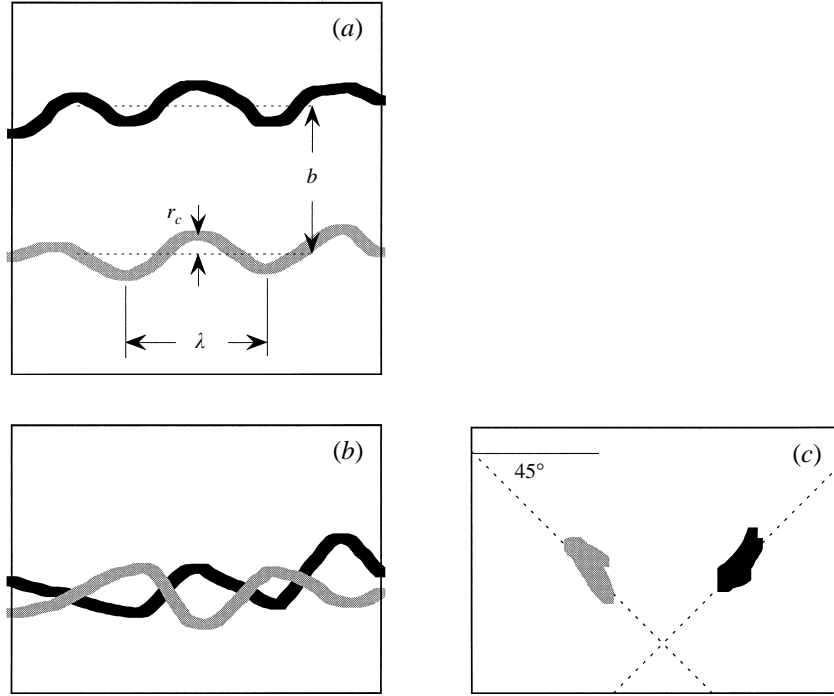


FIGURE 6. Three-dimensional reconstruction of the deformed vortex centreline, from the simultaneous views in figure 5: (a) front view, (b) side view, (c) end view.

to the vorticity, whose maximum value at the centre is about $\Gamma/\pi a^2$. In this case the band of unstable θ is centred around $\theta_o = 60^\circ$, which is the most unstable angle.

Waleffe (1990) showed that solutions with a given k_o and θ could be combined (by integration over t_o) to give disturbances that are localized near the axis of rotation. In addition, these solutions can satisfy certain radial boundary conditions, which is important if one considers a finite region of elliptical flow. For vanishing strain and $\theta = \theta_o$, these solutions take a simple analytical form in cylindrical coordinates (r, φ, z) :

$$u_r = C \frac{\sqrt{3}}{2} e^{\sigma t} [J_0(\sqrt{3}k_z r) + \frac{1}{3}J_2(\sqrt{3}k_z r)] \cos k_z z \sin(\varphi + \frac{1}{4}\pi), \quad (4.4a)$$

$$u_\varphi = C \frac{\sqrt{3}}{2} e^{\sigma t} [J_0(\sqrt{3}k_z r) - \frac{1}{3}J_2(\sqrt{3}k_z r)] \cos k_z z \cos(\varphi + \frac{1}{4}\pi), \quad (4.4b)$$

$$u_z = C e^{\sigma t} J_1(\sqrt{3}k_z r) \sin k_z z \sin(\varphi + \frac{1}{4}\pi). \quad (4.4c)$$

The corresponding components of the vorticity are

$$\omega_r = C \sqrt{3} k_z e^{\sigma t} [J_0(\sqrt{3}k_z r) + \frac{1}{3}J_2(\sqrt{3}k_z r)] \sin k_z z \cos(\varphi + \frac{1}{4}\pi), \quad (4.5a)$$

$$\omega_\varphi = C \sqrt{3} k_z e^{\sigma t} [J_0(\sqrt{3}k_z r) - \frac{1}{3}J_2(\sqrt{3}k_z r)] \sin k_z z \sin(\varphi + \frac{1}{4}\pi), \quad (4.5b)$$

$$\omega_z = C 2 k_z e^{\sigma t} J_1(\sqrt{3}k_z r) \cos k_z z \cos(\varphi + \frac{1}{4}\pi). \quad (4.5c)$$

Here, $k_z = 2\pi/\lambda = k_o \cos \theta$ is the axial wavenumber of the perturbation, the J_i are Bessel functions of the first kind, and C is a constant. For small strains, one can deduce from the results of Landman & Saffman (1987) and Waleffe (1990), that the

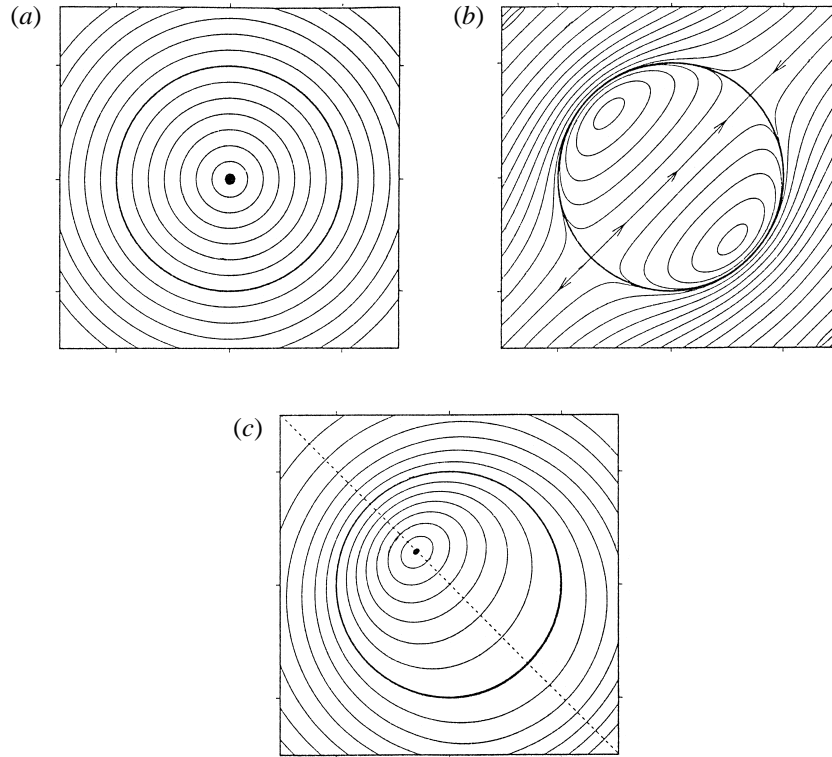


FIGURE 7. Streamlines associated with localized modes of the elliptic instability of a base flow with uniform vorticity, uniform strain with stretching in the -45° direction, and in the limit of vanishing strain: (a) base flow, (b) perturbation (Waleffe 1990), (c) total flow. The perturbation displaces the centre of rotation in the direction of maximum stretching. The bold line marks the invariant streamline.

growth rate (σ) is given by

$$\sigma = \frac{9}{16} \varepsilon - \nu k_o^2. \quad (4.6)$$

In the case of inviscid flow, all wavenumbers k_o have the same growth rate, whereas for finite values of the viscosity (ν) one finds a low-wavelength cut-off.

It is instructive to visualize the spatial structure of the disturbance (4.4) and the modifications it produces in the total flow, i.e. the sum of disturbance and base flow. (The theoretical papers, up to now, illustrated the flow only by the perturbation field. We wish here to predict precisely what one will actually observe and measure in the real flow.) In figure 7(a), we show streamlines of the base flow, which for $\varepsilon = 0$ is simply a solid-body counter-clockwise rotation, and in figure 7(b) we show the perturbation given by (4.4), which has a very characteristic shape. In particular, there exists a distinct circular streamline with zero radial velocity, which means that the streamline of the base flow that has the same radius will remain unaffected by the perturbation ('invariant'). Streamlines of the total flow are given in figure 7(c). They show that the centre of rotation is displaced in the direction of maximum stretching of the (infinitesimal) strain field, and that the layers inside and outside the 'invariant streamline' are displaced in opposite radial directions. The pattern in figure 7(c) is modulated in the axial direction. A longitudinal cut through the vortex in the stretching plane is given in figure 8, showing the displacement of the vortex centre

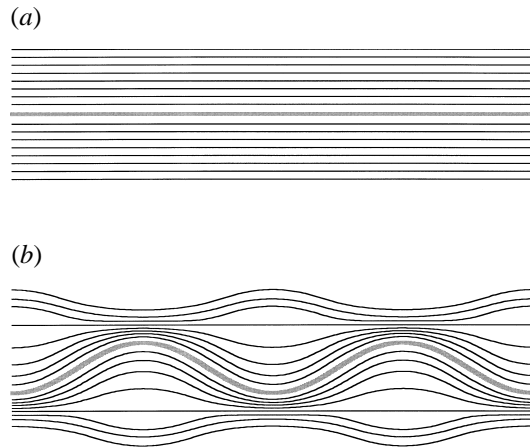


FIGURE 8. Longitudinal cut through stream surfaces of (a) the unperturbed and (b) perturbed vortex, according to theoretical predictions. The position of the cut is marked by the dashed line in figure 7(c).

and the invariant stream tube. The diameter d_{inv} of this tube can be determined by finding the first zero of the radial perturbation velocity (4.4a): $u_r(r = d_{inv}/2) = 0$. This leads to $\sqrt{3}k_z d_{inv}/2 = 2.7346$, or

$$\lambda/d_{inv} = \frac{\sqrt{3}\pi}{2.7346} = 1.9898 \quad (\text{theoretical}), \quad (4.7)$$

i.e. the axial wavelength is almost precisely twice as large as the diameter of the invariant streamline. This result, as well as figures 7(c) and 8(b), can be compared to experimental observations.

Before making such a comparison, however, we would like to consider the effect of a finite domain size on the elliptic instability. A radial confinement imposes boundary conditions on the base flow and the perturbations, which, in general, select a discrete set of radial scales out of the continuum allowed in an infinite domain. The same applies in principle in the axial direction, but since we are dealing with slender vortices whose lengths are large compared to the core diameters (ratio > 150), the radial confinement has the dominant effect. Since the radial and axial scales are linked through the wave vector inclination θ (see equation (4.3)), and only a small interval of θ around 60° leads to instability, this implies that a discrete set of bands of unstable axial wavenumbers are selected by the radial boundary conditions. One example of (inviscid) boundary conditions was considered by Waleffe (1990): the flow inside a rigid cylinder of almost circular cross-section. He found the admissible perturbations by matching the cylinder radius with the radius of the invariant streamline.

A different kind of confinement is given in a columnar (or Rankine) vortex, with a circular core (radius a_R) of constant vorticity surrounded by irrotational fluid. Here, the boundary of the vortical fluid is not rigid or impermeable. This flow was treated by Kelvin (1880), who analysed the vortex stability with respect to disturbances proportional to $\exp[\sigma t + i(m\varphi + k_z z)]$ for the case of pure rotation without strain. He found that σ is always imaginary and that the flow is therefore (marginally) stable; all perturbations simply rotate around the vortex. His dispersion relation, which gives the rotation rate as function of the axial wavenumber, is found from the dynamic and kinematic boundary conditions at the edge of the core. A discussion of the dispersion

relation and the different perturbation modes can be found in Saffman (1992). Of special interest for the present study are the modes with azimuthal wavenumbers $m = \pm 1$, which correspond to different kinds of vortex bending. For this case (as for the other m), Kelvin's (1880) dispersion relation admits only discrete branches, shown, for example, by Widnall *et al.* (1974), each corresponding to a different radial scale and structure of the velocity field. When these modes are numbered by n , the perturbation corresponding to $n = 0$ is a simple displacement of the entire core and can be associated with Crow's (1970) long-wavelength instability. The higher-order bending modes with $n \geq 1$ have a more complicated radial structure leading to internal deformations of the vortical core. Concerning the short-wavelength instability, Widnall *et al.* (1974) proposed that these higher modes would lead to instability in the presence of a straining field, whenever their rotation rate in the unstrained case is zero, or close to zero. For each radial mode n (≥ 1), this happens at and around a distinct axial wavenumber k_n . For the Rankine vortex, the first three of these k_n are:

$$k_1 = \frac{2.5}{a_R}, \quad k_2 = \frac{4.4}{a_R}, \quad k_3 = \frac{6.2}{a_R}. \quad (4.8)$$

We now deduce, with much relevance to this study, that, *inside the core* ($r < a_R$), *the disturbance flow field of a Kelvin mode $n \geq 1$ with $k_z = k_n$ is identical to the most unstable elliptic instability perturbation with the same wavenumber, in the low-strain limit* (equations (4.4) and (4.5)). In particular, for a given mode n , there exist n concentric invariant stream surfaces inside the core. In the irrotational fluid outside the core, the disturbances decay smoothly without further oscillations in the radial direction (Kelvin 1880). As mentioned above, the discrete unstable axial wavenumbers thus selected by the boundary conditions open up to narrow bands of instability for finite strain, as shown by the numerical studies of Tsai & Widnall (1976) and later Robinson & Saffman (1984). To leading order, the spatial structure of the perturbations remains the same for small strain.

Tsai & Widnall (1976) also calculated the growth rate of the most unstable modes in each band of unstable wavenumbers for inviscid flow and small but non-zero strain and found $\sigma \approx 0.57\varepsilon$ for $n = 1, 2$. This is extremely close to the value $\sigma = (9/16)\varepsilon = 0.5625\varepsilon$ for the elliptic instability (equation (4.6)), and also seems to depend only weakly on the band (n) considered.

In summary, the results discussed in this section suggest rather strongly that the short-wavelength instability of a strained vortex studied by Tsai & Widnall (1976) is indeed an elliptic instability in a finite domain, the vortex core. It is surprising, however, that the spatial structure of the most unstable perturbations, as well as their growth rates, seem to be almost unaffected by the finite size of the elliptical flow region. In the remaining part of this section, elements of both theories will be used for comparison with our experimental results.

4.2. Spatial structure of the instability mode

We now return to experimental observations concerning the short-wavelength instability in a pair of vortices. A real vortex presents two important differences with the Rankine vortex model treated by Kelvin (1880) and Widnall *et al.* (1974). First, the vorticity distribution is not a step function, but it is a smooth distribution and more closely represented by an Oseen vortex, as seen in §2. The qualitative features of the instability, linked to the finite size of the core, can be expected to be similar in this case, but the different 'boundary conditions' (the core boundary is actually

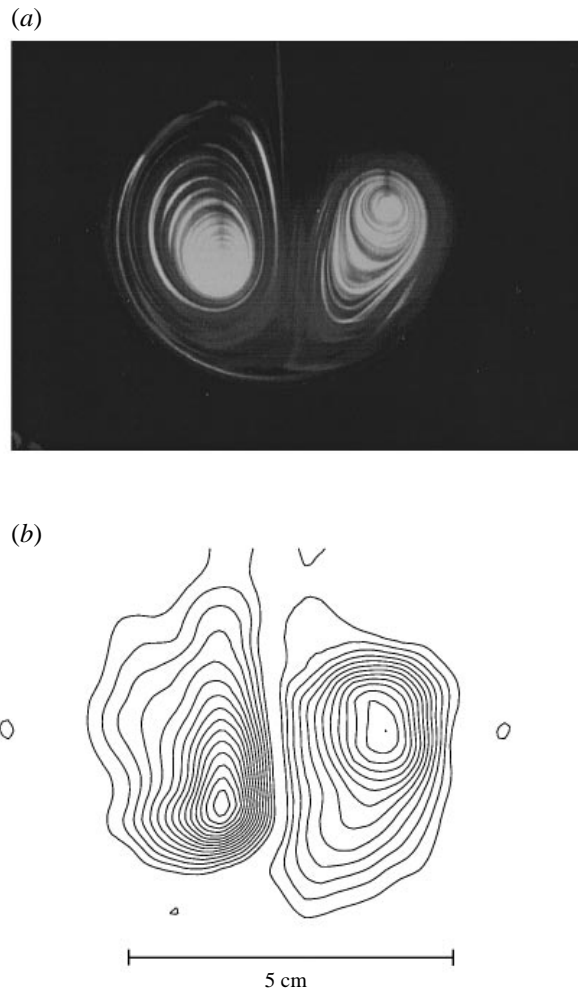


FIGURE 9. Perturbation in a cross-cut plane due to the short-wavelength instability at $Re = 2400$: (a) dye visualization at $t^* \approx 7.5$; (b) vorticity contours obtained from DPIV measurements made at approximately the same time.

not very well defined in a real vortex) are likely to select a different set of unstable wavenumbers or wavenumber bands. The question of how the instability scales on the parameters of a real vortex, in particular the core parameter a , is answered with the help of experimental results, as shown below.

The second difference is the non-vanishing viscosity. Equation (4.6) shows that viscosity reduces the growth rate of the elliptic instability for larger wavenumbers. This means that, of all unstable perturbations compatible with the boundary conditions, *the perturbation with the smallest wavenumber (largest wavelength) is the most unstable*, and should be observed in an experiment. For the finite-core vortex this is the second radial bending mode with $n = 1$, whose streamlines in a cross-sectional view are given in figure 7.

Figure 9(a) shows an experimental visualization of the vortex pair cross-section at a time when the short-wave instability is already well developed. A displacement of the vortex centres is observed, which is very similar to the theoretical prediction

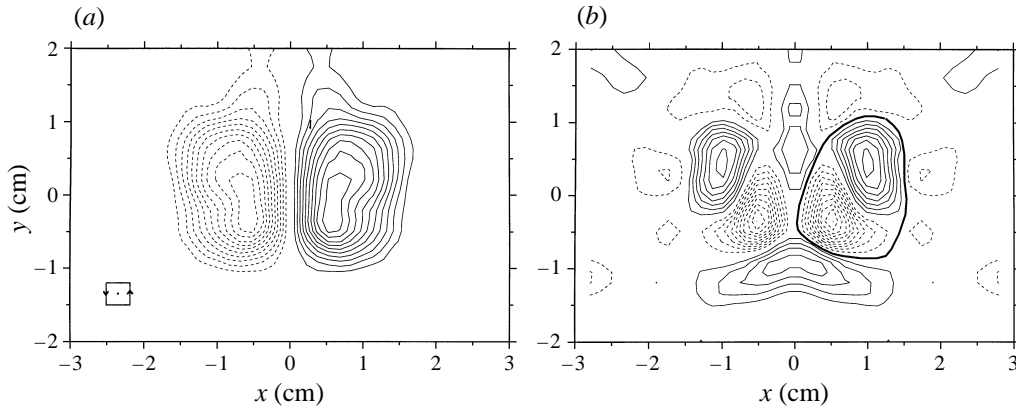


FIGURE 10. Decomposition of the measured axial vorticity in figure 9(b) into: (a) the antisymmetric (with respect to the plane $x = 0$) distribution of the vortex pair base flow, and (b) the symmetric perturbation vorticity. (The square in (a) represents the size of the contour used to calculate the vorticity by the circulation method.) The bold line in (b) corresponds approximately to zero perturbation vorticity. Its diameter is about 50% bigger than the initial core diameter $2a \approx 1$ cm. Contour spacing in (a) as in figure 24, in (b) twice as dense.

in figure 7(c): to the lower right in the left-hand vortex, and to the upper right in the right-hand one, i.e. in the respective stretching directions of the mutually induced strain. That this distortion is not simply an effect of the advection of the dye is demonstrated in figure 9(b), where the corresponding vorticity contours, determined from DPIV velocity measurements, are given. They show the same characteristic deformation. The cross-sectional view in figure 9(a) complements the visualizations from the front and side in figure 5 and demonstrates again the symmetry breaking of the total flow due to the short-wave perturbation, which is further discussed in §4.4.

The fact that the base flow of a counter-rotating vortex pair has an antisymmetric vorticity distribution can be used to find the actual (symmetric) perturbation of axial vorticity associated with the instability. Figure 10 shows the decomposition of the vorticity field in figure 9(b) with respect to the vertical line of symmetry of the initial pair. (Small quantitative, but certainly no qualitative, changes could be incurred by visual errors in setting up the position and orientation of this line. Here, we are interested in the qualitative features of the perturbation.) The perturbation in figure 10(b) exhibits a characteristic two-lobe structure in each vortex, with the maxima aligned in the stretching direction. This is strikingly similar to the theoretical perturbation vorticity for the elliptic instability, shown by Waleffe (1990, figure 2) and whose analytical expression is given by equation (4.5c).

In the front or side views an equally good correspondence is found between experiment and theory. In the visualization in figure 11, the internal structure of each vortex is almost identical to the prediction in figure 8(b). In particular, the existence of an invariant stream surface is clearly seen. The distributions of azimuthal vorticity in a plane containing the axis of one vortex can also be compared. The theoretical prediction for the second radial bending mode of a Rankine vortex is shown in figure 12, deduced from Kelvin's (1880) results. The corresponding experimental measurements of azimuthal vorticity in figure 13 were made in a vertical plane and show a very similar three-lobe checkerboard pattern.

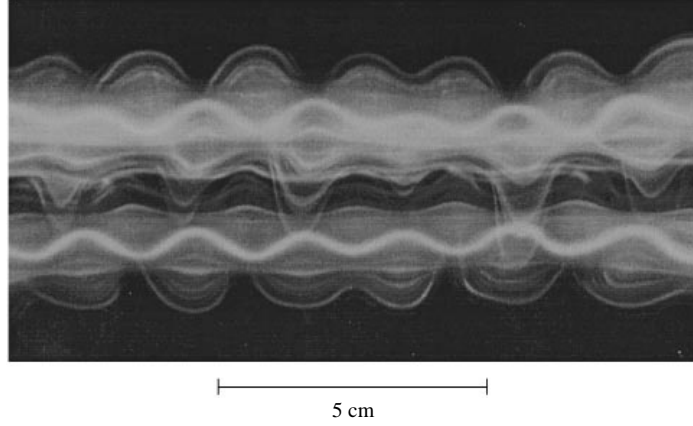


FIGURE 11. Close-up view of the short-wavelength perturbation, showing the characteristic internal vortex deformations, as well as the distinct phase relationship between the perturbations of the two vortices. $Re = 2750$, $t^* = 6.2$.

4.3. Scalings

The previous subsection has shown that, despite the non-uniform vorticity (and strain) inside the vortex cores, the observed instability has a structure which is very similar to the one predicted for the elliptic instability of a Rankine vortex. Furthermore, it can easily be measured from visualizations like figure 11 that the wavelength is also very nearly twice the diameter of the invariant stream tube,

$$\lambda/d_{inv} = 2.0 \pm 0.1 \quad (\text{experimental}), \quad (4.9)$$

which closely matches the theoretical relation (4.7). Thus, the ‘aspect ratio’ of the perturbation found experimentally is almost precisely what is predicted from elliptic instability theory. (One should note that errors in this and other measurements are discussed in §2.)

A further question is how one may relate the size of the perturbation to the size of the vortex. We determine it here experimentally, using flow visualization like figure 11 to obtain d_{inv} and DPIV measurements under identical conditions to find the core size a in (2.1). To experimental accuracy, the result of these measurements is

$$d_{inv}/a = 2.0 \pm 0.1, \quad (4.10)$$

which, together with (4.10), gives

$$\lambda/a = 4.0 \pm 0.4 \quad (4.11a)$$

or

$$k_z a = 1.6 \pm 0.2. \quad (4.11b)$$

This can be compared to the result for a Rankine vortex, for which $k_1 a_R = 2.5$ and, using (4.9), the diameter of the invariant streamline is found to be $d_{inv} = 1.3a_R$. The result in (4.10) and (4.11), which is deduced from streamlines and velocity data, is also consistent with the scales of the vorticity distribution in figures 10 and 13. From the analytical expressions in (4.5c) one finds that the diameter of the line (or tube) of invariant axial vorticity is 40% bigger than that of the invariant streamline. In figure 10(b), this line is shown as determined from experiment; its diameter is indeed significantly bigger than the initial core diameter $2a$, which is approximately equal

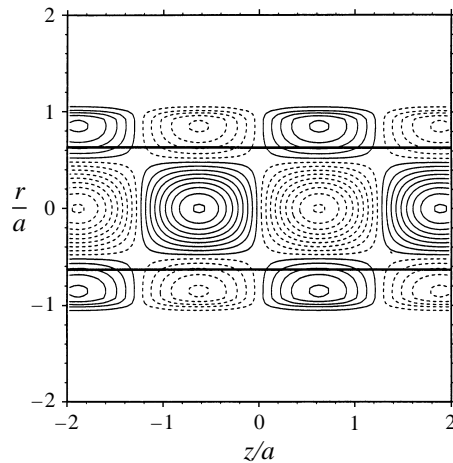


FIGURE 12. Azimuthal vorticity of the 'second radial mode' perturbation in a vortex with finite core size, deduced from Kelvin (1880). In the presence of a plane strain, this mode is the most unstable. The plane shown here would then be oriented in the compression direction of the strain. The straight lines indicate the location of the invariant stream tube. Coordinates are given in units of the core radius a_R .

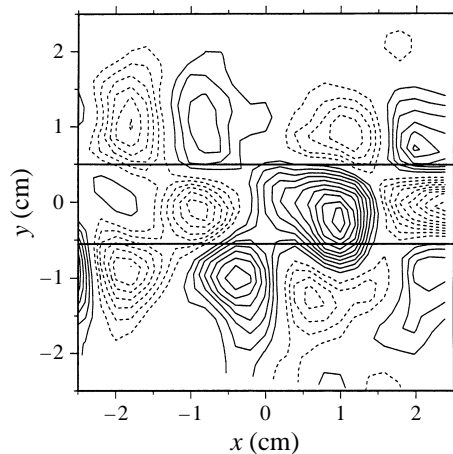


FIGURE 13. Azimuthal vorticity in a plane cutting through one of the vortices, measured with DPIV. The spacing of the straight lines corresponds to the diameter of the invariant stream tube, measured independently from flow visualizations.

to d_{inv} according to (4.10). Similarly, the tube of the invariant azimuthal vorticity is predicted from (4.5b) to have a diameter of about 20% less than the invariant stream tube (see also figure 12). Even if this diameter cannot be determined very accurately in the measurement of figure 13, this prediction seems reasonably well matched.

Three theoretical results concerning the instability of vortices with smooth vorticity profiles may be mentioned. Widnall, Bliss & Zalay (1971) showed that, for the first bending mode ($n = 0$) and long axial wavelengths ($k_z a < 0.5$), a vortex with an arbitrary axisymmetric velocity profile could be associated with an equivalent Rankine vortex having the same rotation rate, and therefore showing the same long-wavelength instability characteristics in the case of a vortex pair or other external

strain field. The core radius a_e of this equivalent Rankine vortex is a function of the velocity profile; for the case of an Oseen vortex (2.1) it is found to be

$$a_e = 1.36 a. \quad (4.12)$$

If one assumes that a similar relation holds for the higher bending modes (although this is not at all guaranteed), and then uses (4.8) for the equivalent vortex (with $a_R = a_e$), one obtains $k_z a = 1.8$, which is reasonably close to the experimentally determined result (4.11b).

Secondly, Widnall *et al.* (1974) have determined numerically the dispersion relation for a vortex with a fourth-order-polynomial vorticity distribution, $\omega_z(r) = (r^2 - a_1^2)^2$, and found that the second radial mode has zero rotation for $k_z a_1 = 3.9$. This vorticity profile can be closely fitted by an Oseen-type Gaussian profile with a core size $a = 0.6a_1$, so that, in the presence of a strain, one would expect a short-wavelength instability for $k_z a = 2.3$.

4.4. Phase relationship of the cooperative instability

The symmetry-breaking phase relationship between the disturbances on both vortices shown in §3 cannot be explained from the existing theories on the instability of a single vortex in a two-dimensional strain field. Instead, to explain the cooperative development of the two instabilities, one has to consider the effect of the perturbations of each vortex on the strain it induces on the other vortex, and their mutual interaction. If one only looks at the displacements of the vortex centres as shown in figures 5 and 6, they have the same symmetry as the antisymmetric mode of instability found in a vortex pair by Crow (1970). This may give a clue to the understanding of the short-wave symmetry.

In Crow's (1970) analysis, he calculated the net effect on a perturbed vortex filament resulting from its self-induced rotation, coupled with the induced velocity on this vortex due to the perturbations on the second vortex. As mentioned in §1, the expression used by Crow (1970) for the self-induced rotation is not valid for the short wavelengths for which he found the antisymmetric (and another symmetric) instability mode. However, if one replaces his expression with the relation for the $n = 1$ bending mode, and if one further assumes that the velocity that a first vortex induces on the second vortex is mainly determined by the region of high vorticity for the first vortex, i.e. close to the centreline, one ends up with a problem qualitatively similar to the one treated by Crow (1970). One would therefore expect both symmetric and antisymmetric instabilities to occur at a wavelength for which the self-induced rotation vanishes, i.e. for $k_z = k_1$.

The fact that only the antisymmetric mode is observed in our vortex pairs is caused by two factors. First, following Crow's (1970) analysis, the antisymmetric mode has a slightly higher growth rate. Second, and more importantly, it is the only one that can fulfil the kinematic boundary condition in the plane separating the two vortices, which imposes a matching of the normal velocity components on both sides of this plane. Here, we consider the disturbance velocities at the outer part of the finite vortices.

The result from the matching of the perturbations of the two vortices is easily illustrated for the point halfway between the unperturbed vortex centres. If the pair is oriented as in figures 9 and 10, and local cylindrical coordinates (r_L, φ_L, z) and (r_R, φ_R, z) are introduced for the left- and right-hand vortex, respectively, then the

matching condition reads

$$u_r^{left}(r_L = b/2, \varphi_L = 0, z) = -u_r^{right}(r_R = b/2, \varphi_R = \pi, z). \quad (4.13)$$

We saw in §4.2 that the observed perturbations correspond closely to the theoretical predictions in (4.4) and (4.5). Taking into account the orientation of the stretching axes in the -45° and $+45^\circ$ directions for the left- and right-hand vortex, the radial velocity perturbations have then the form

$$u_r^{left} = f(r_L) \cos(k_z z) \sin(\varphi_L + \frac{1}{4}\pi), \quad (4.14a)$$

$$u_r^{right} = f(r_R) \cos(k_z z + \phi) \sin(\varphi_R - \frac{1}{4}\pi). \quad (4.14b)$$

The radial dependence $f(r)$ is different from the one in (4.4a) outside the vortical cores (see Kelvin 1880), but this is not relevant here. Condition (4.13) is only fulfilled when the axial phase difference is $\phi = \pi$. From the corresponding expressions for the axial vorticity disturbance in (4.5c), it is straightforward to see that these theoretical kinematical conditions correspond to the experimental perturbation symmetry shown in figure 10(b), which lead to the observed antisymmetric deformation of the vortex centrelines.

4.5. Growth rate

The experimental determination of the growth rate of the short-wave instability is faced with two difficulties: the simultaneous development of the long-wavelength Crow instability (see figure 4), which modulates the short waves, and the fact that the perturbation flow field (4.4) shown in figure 7(b) is not directly accessible and cannot be deduced precisely early in the evolution, especially as a function of time. The first problem was solved by recording a large number of runs until, by chance, the initial background noise was such that the amplitude of the long-wave instability remained at a sufficiently low level during the growth of the short waves. This situation had to be verified by flow visualization along the vortex axis, which in turn precluded the use of DPIV for the measurement of the disturbance field. However, the amplitude of the vortex centre displacement (r_c) could be determined quite accurately from the visualizations, typified by figure 11.

Using (4.4a,b), the theoretical displacement resulting from an exponentially growing perturbation was calculated numerically and is shown in figure 14(a). After an initially exponential growth, the displacement saturates at an asymptotic value. The intermediate evolution, corresponding to the measurable range of amplitudes before the regular pattern breaks down, is almost linear in time, with the slope depending on the growth rate. Considering an exponential disturbance growth even for finite amplitudes is not unreasonable, since the waves (4.2) that make up the disturbances are solutions to the full, nonlinearized disturbance equations (Landman & Saffman 1987; see also Craik & Criminale 1986). Figure 14(b) shows the measured amplitudes, taking into account at least 16 wavelengths for each point. The results are consistent with the assumed linear variation, and a least-squares fit to the theoretical curve yields a non-dimensional growth rate

$$\frac{\sigma}{\Gamma/2\pi b^2} = 0.94 \pm 0.12, \quad (4.15)$$

obtained for a non-dimensional wavelength of $\lambda/b = 0.77 \pm 0.02$. We cannot claim that (4.15) represents the growth rates in the majority of experiments where the long-wavelength Crow instability is strongly interacting with the short-wave instability. We reiterate that the Crow instability leads to a modulation of the vortex spacing and

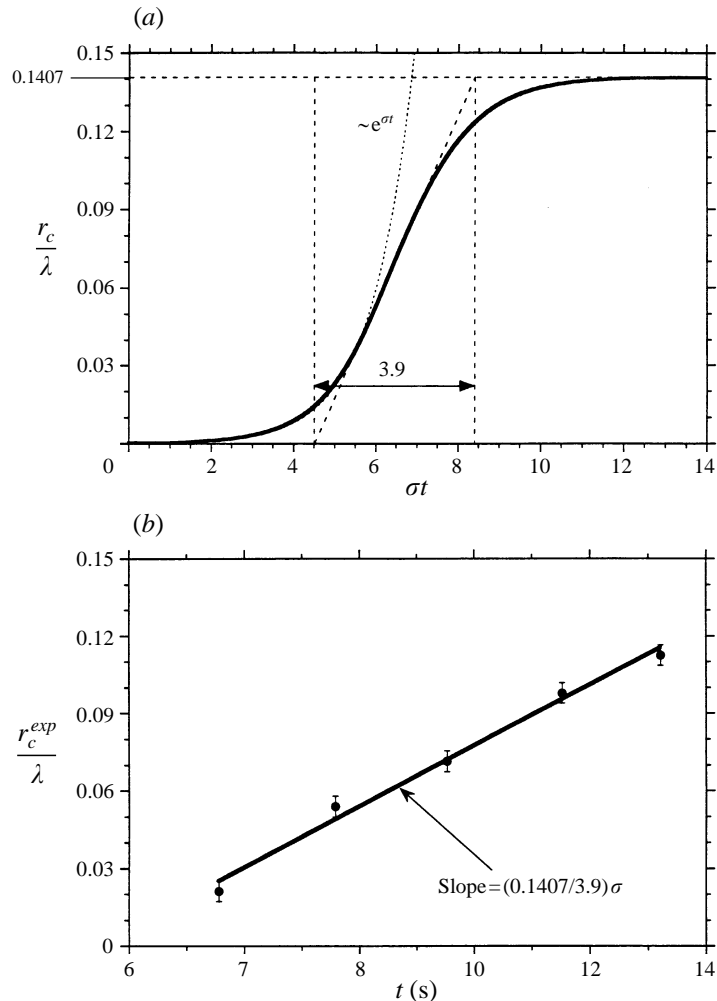


FIGURE 14. Displacement of the vortex centres in time due to elliptic instability, seen in front view (compare figure 6a). (a) Theoretical prediction for an exponentially growing perturbation, obtained numerically using the analytical expressions given by Waleffe (1990). The origin of time is arbitrary. (b) Experimental measurements from visualizations as in figure 11.

the mutually induced strain, which makes it difficult to define a (single) short-wave growth rate in this case. However, in the experiment discussed in this paragraph, the vortices were parallel (to within 5% of the mean vortex spacing), so that (4.15), even if it comes from a rare experiment, represents the growth rate of a ‘pure’ short-wave (elliptic) instability, which, so far, had never been measured experimentally.

The quantity $\Gamma/2\pi b^2$ is the magnitude of the strain induced by one vortex at the location of the other vortex *if this other vortex was not there*. It is an exterior strain ε_{ext} . Since Crow (1970), it has been used in a standard way to non-dimensionalize growth rates of vortex pair instabilities. However, it should be made clear that it is *not* the strain present in the cores of an actual vortex pair. Moore & Saffman (1971) calculated the response of a Rankine vortex to an imposed exterior strain. One result is that the circular shape of the core is distorted into an ellipse whose major axis is tilted 45° to the stretching axis (see also Robinson & Saffman 1984). This is

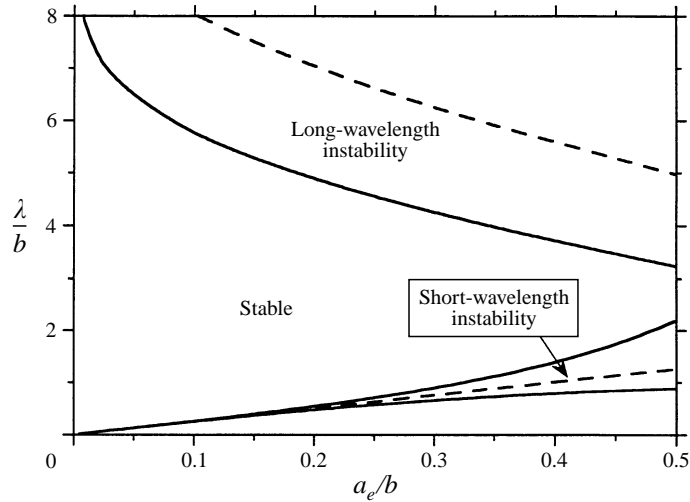


FIGURE 15. Stability diagram for a pair of Rankine vortices with core radius a_e , showing the domains of long-wavelength instability (after Crow 1970) and the second-radial-mode short-wavelength instability (Tsai & Widnall 1976). Dashed lines show the wavelengths for maximum amplification.

confirmed by our measurements later in figures 24(a) and 25(a), where the initial vorticity distributions are seen to be slightly elongated vertically. Furthermore, it can be deduced from their study that the *interior* strain ε close to the centre is precisely twice as high as the imposed exterior strain: $\varepsilon = 2\varepsilon_{ext}$. Experimental measurements of the strain magnitude in the cores using DPIV are not very precise, but the same order of magnitude is found for the ratio between interior and induced exterior strain. This difference has to be taken into account when comparing to the elliptic instability, since it is the interior strain that determines the ellipticity of the streamlines and the growth rate in (4.6).

The experimental result (4.15) can be compared to the different theoretical predictions. In figure 15, the domains of long- and short-wavelength instability for a pair of inviscid Rankine vortices are shown. The long-wave stability limit was calculated in Leweke & Williamson (1998a) using the exact result for the self-induced rotation. The result for short waves was deduced directly from Tsai & Widnall's (1976) numerical results concerning the unstable wavenumber band for the second radial bending mode (or $n = 1$ mode). The initial core size of the vortices in the experiment was given by $a/b = 0.2$, corresponding to an equivalent Rankine vortex of radius $a_e/b = 0.27$ (see equation (4.12), where this equivalent radius is discussed). The inviscid growth rates of the two instabilities along this line in the stability diagram is given in figure 16, together with the experimental value. The agreement for the short waves is quite good. According to (4.6), viscosity reduces the growth rate, which is why the lower experimental value is not surprising.

The experimental growth rate may also be compared with predictions from elliptic instability theory, in this case involving viscosity, as follows. Using $\varepsilon = \Gamma/\pi b^2$ (see above) and $k_o = k_z/\cos\theta$, with $\theta = 60^\circ$ for low strain, (4.6) can be rewritten as

$$\frac{\sigma}{\Gamma/2\pi b^2} = \frac{9}{8} - \frac{32\pi^2}{(\lambda/b)^2 Re}, \quad (4.16)$$

giving the viscous growth rate as function of Reynolds number and instability wave-

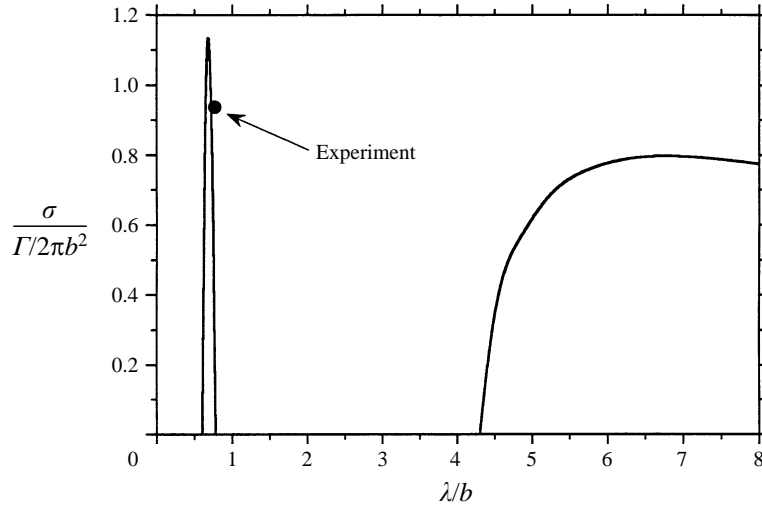


FIGURE 16. Inviscid growth rates of long- and short-wavelength instabilities for $a_c/b = 0.27$, corresponding to a pair of Oseen vortices with radius $a/b = 0.2$.

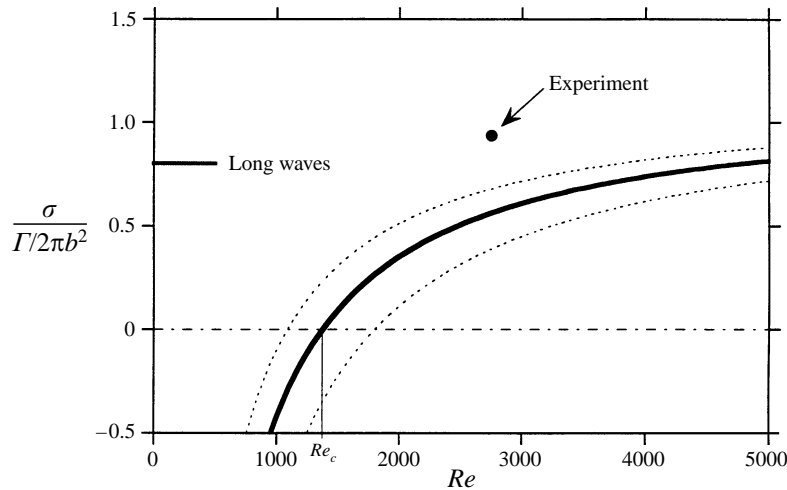


FIGURE 17. Viscous growth rate of elliptic instability in a vortex pair as function of Reynolds number for $\lambda/b = 0.8$ (deduced from Landman & Saffman 1987). The curves for $\lambda/b = 0.9$ (upper dotted line) and $\lambda/b = 0.7$ (lower line) are also given. The growth rate of the long-wavelength instability is independent of Re .

length. The resulting curve for the experimental λ is plotted in figure 17. Considering the idealized nature of the theoretical flow, the comparison of the experimental and theoretical growth rates is quite satisfactory.

Figure 17 and the relation (4.16) also show that, for a given wavelength, which is imposed by the radial boundary conditions, there exists a critical Reynolds number Re_c for the short-wavelength elliptic instability, which can be found from $\sigma(Re_c) = 0$:

$$Re_c = \frac{2^8 \pi^3}{9 (\lambda/b)^2} \approx \frac{16\pi^3}{9 (a/b)^2}. \quad (4.17)$$

Below Re_c , the perturbation is damped and the flow is stable. The last relation in

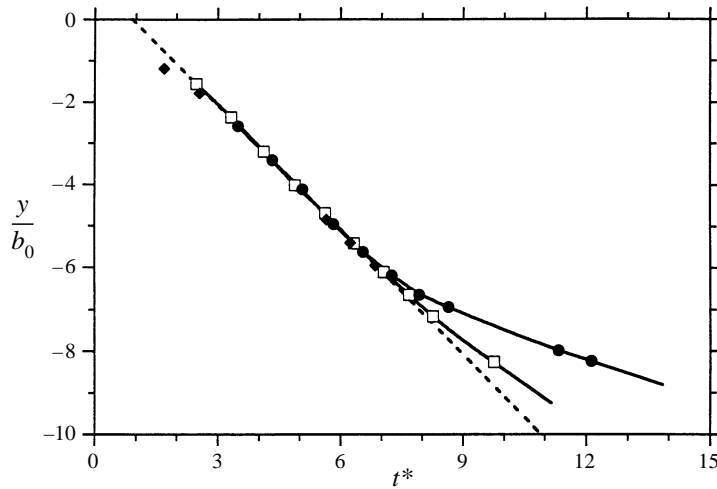


FIGURE 18. Average vertical position of the vortex pair as a function of time, for two cases. (i) In the presence of a large-scale (Crow) instability (filled symbols); the descent speed decreases by about 65% the break-up of the short-wavelength perturbation. (ii) In the absence of a long-wavelength instability (open symbols); the descent speed decreases much more slowly. $Re \approx 2700$.

(4.17) is found from the experimental result (4.11a). Another interpretation of (4.17) is that, at a given Re , the instability will not manifest itself unless the size a of the region with elliptical flow exceeds a certain minimum.

5. Long-term evolution

After having explored the origin and early stages of the short-wave vortex pair instability, we now investigate the later evolution of the flow, in which the interaction with the long-wavelength instability becomes important.

The fact that, at a certain point, a significant change is occurring in the flow is illustrated by the evolution of the overall descending motion of the pair. In figure 18 the average vertical position of the pair, measured from side-view photographs, is plotted. The filled symbols show the result for the general case where both short and long waves develop simultaneously. Up to a non-dimensional time $t^* \approx 6$, which corresponds approximately to the time of figure 4(b), the descent speed is constant. The pair then slows down considerably over a short period of time, and finally continues to move down at a speed which is about 1/3 of the initial speed. The open symbols represent one of the rare cases where the long waves do not develop significantly. The behaviour is very similar in the beginning, but the final speed is noticeably higher in this case.

The origin of this change in the flow lies in the breakdown of the complicated, but nevertheless organized disturbance structure described in §4.2, which begins approximately at the time when the pair starts to slow down. The visualizations in figure 19 show the early stages of this breakdown. In figure 19(a), we see that, near the front edge of the pair, the parts of the fluid initially orbiting each vortex individually begin to mix. In a periodic interlocking way, tongues of fluid from one side are drawn around the respective other vortex.

This cross-over is a direct consequence of the internal vortex deformations, and can be illustrated with the help of figure 9. On the one hand, the centre of rotation

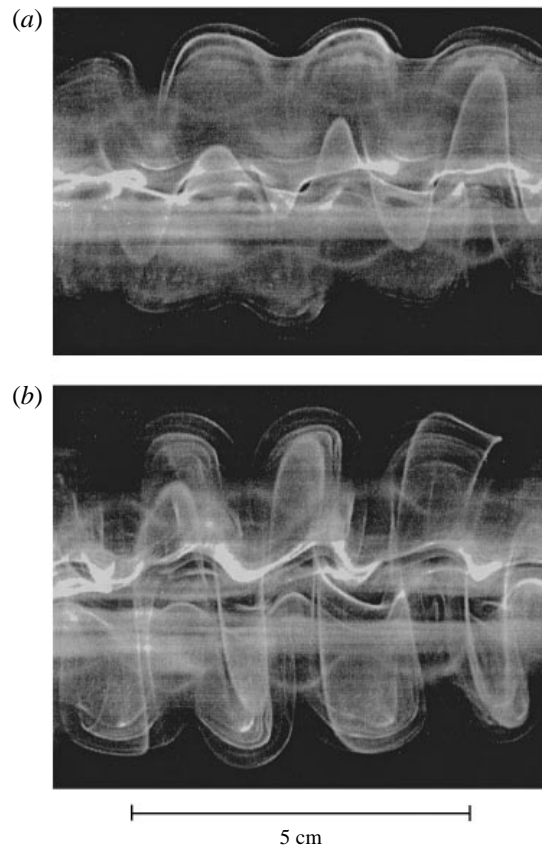


FIGURE 19. Consecutive close-up views of the breakdown of the short-wavelength perturbation. The vortex pair is moving towards the observer. In (a), tongues of fluid initially orbiting one vortex are drawn around the other one. These tongues are stretched into secondary vortex pairs in (b).

(maximum of vorticity) of the left-hand vortex is displaced toward the front stagnation point, whereas the one on the right is pushed away. On the other hand, we know that the outer layers of each vortex are displaced in opposite directions. This means that the outer parts of the right-hand vortex are actually brought closer to the stagnation point, and to the approaching left-hand vorticity maximum; the latter will eventually capture some of this fluid and pull it to the left. The vortex centrelines are also faintly visible in figure 19(a), and the phase of their displacement is consistent with this scenario. Owing to the orientation of the deformation (see figure 6c), which is linked to the stretching axes of the strain, it is clear that this phenomenon can only occur at the leading edge of the pair.

Once the tongues have crossed over, they are quickly pulled apart by the stagnation-point flow and wrapped around the primary vortices (figure 19b). This results in the formation of an array of transverse counter-rotating secondary vortex pairs. Figure 9(b) reveals that axial vorticity is pulled to the left with the fluid, and is subsequently tilted and stretched by the stagnation-point strain field. By this process the circulation of the primary vortices is reduced, which could explain the decrease in the self-induced translation velocity of the pair observed in figure 18.

In figure 20, the same phenomenon is seen from the side. The wavelength of the initial elliptic instability can still be identified from the inner core deformation, which,

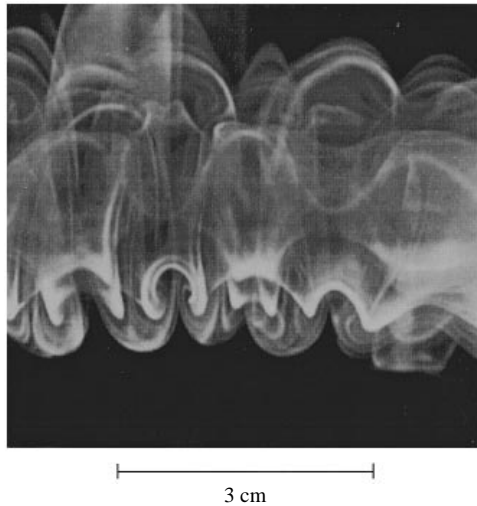


FIGURE 20. Side view of the short-wavelength breakdown, visualized with floodlight illumination. The wavy deformation of the vortex centreline is still visible. For each perturbation wavelength, two secondary vortex pairs are generated at the lower ‘leading edge’ of the primary pair.

at this point, is still relatively ordered. This view shows that, for each wavelength, two secondary vortex pairs are generated at the lower edge. Their development and intensity can be appreciated even better in the light-sheet visualization of figure 21.

The formation of the secondary vortex pairs has a strong effect on the further development of the overall flow. It was found in §3 (figure 4) that the elliptic instability develops faster where the Crow instability brings the vortices together. At these periodic locations along the axes, the organized structure of the primary vortices breaks down first, due to the presence of the perpendicular vortices in the outer layers.

The next steps in the vortex pair evolution are visualized in figure 22. It appears that the primary vortices are stripped of these outer layers, which seem to move away from where the Crow instability pulls the pair together, to leave only a skeleton of the initial vortex pair. One might interpret this axial flow as a consequence of a pressure gradient set up between the less coherent primary vortex in the regions of break-up and the more coherent parts of the vortex not yet broken up. This process may be seen as the result of an ‘attempted’ vortex reconnection, a phenomenon which, in the absence of short waves, leads to periodic vortex rings (Lewke & Williamson 1998 *a*). As a result of this axial motion, the dyed fluid concentrates in large clusters, whose internal motion is apparently relatively unorganized, and whose spacing is dictated by the initial large-scale Crow instability. The same sequence of events is seen in figure 23 in side view: we can see the very regular elliptic disturbance, the breakdown at one particular point along the axis, and the axial motion of vortical fluid into periodic regions of small-scale motion, linked by thin bridges of vorticity.

This late-time development of a vortex pair in the presence of both instabilities is quite different from the case with the Crow instability alone. In the latter instance, the vortices undergo a complete reconnection process leading to a periodic array of vortex rings, which persist for very long times. This means that most of the initial circulation is conserved in long-lived large-scale structures, which is supported by the observation that the average descent speed of the vortices remains approximately

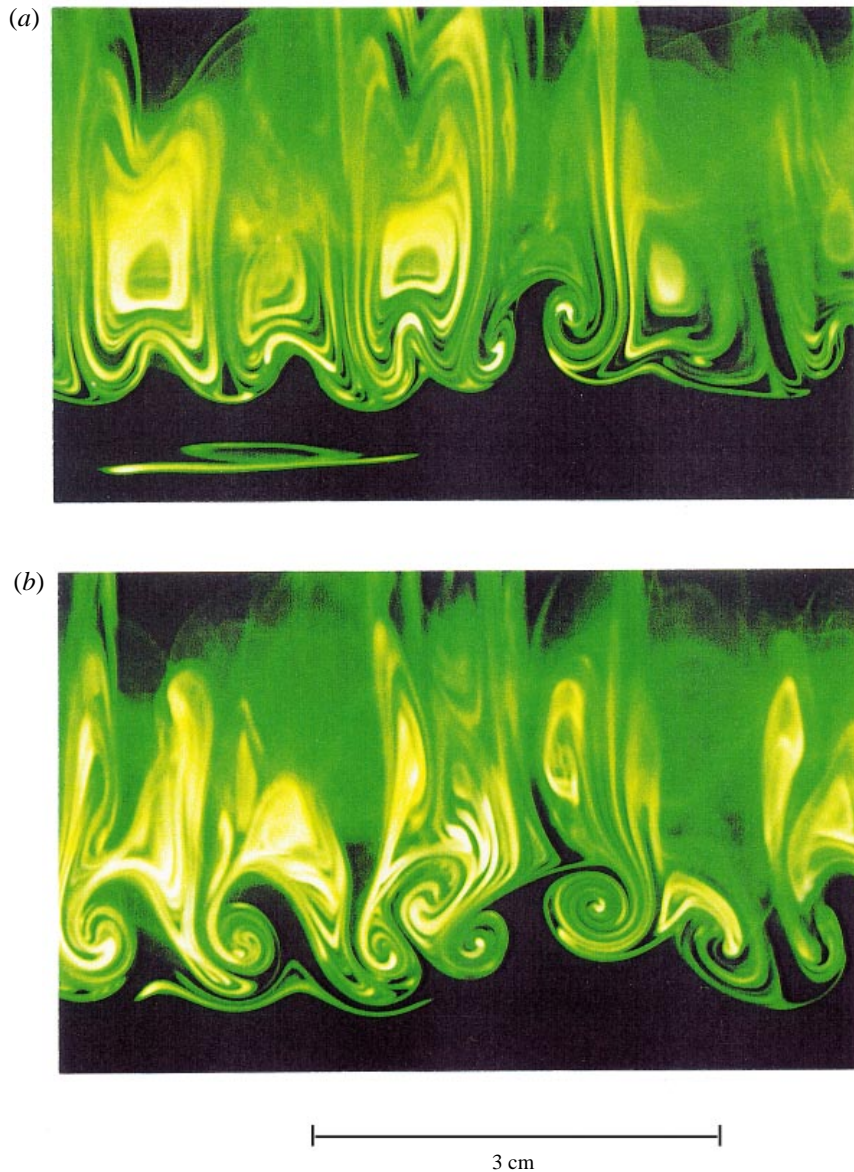


FIGURE 21. Consecutive side views of the short-wavelength breakdown, visualized by a light sheet in the plane initially separating the two vortices.

constant (Leweke & Williamson 1998 *a*). For the present case with a simultaneous short-wavelength instability, figures 22 and 23 suggest that the interaction between the two phenomena enhances mixing and distributes the initial large-scale energy to the small scales much more effectively.

This qualitative observation from flow visualization can be made more quantitative by measuring the actual vortex circulation. For this purpose, sequences of DPIV measurements were made in the cross-plane of the vortices. The camera was moved with the translating pair in a step motion, since measurements from different runs

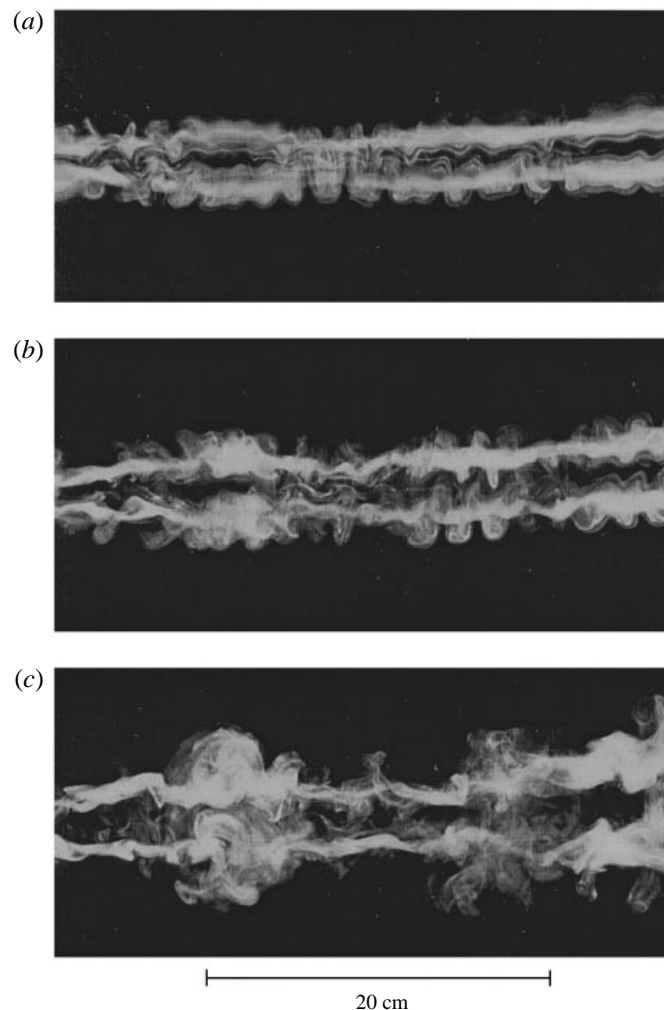


FIGURE 22. Late-time evolution of a vortex pair with both short- and long-wavelength instabilities. $Re = 2750$. The pair is moving towards the observer. (a) $t^* = 7.2$, (b) $t^* = 8.6$, (c) $t^* = 12.1$.

could not be combined due to the random phase of the instability at the measurement position in each run.

Two sequences of vorticity distributions resulting from these measurements are presented in figures 24 and 25. The first sequence, in figure 24 (from which figure 9b is taken), shows the flow in a plane where the vortices approach each other, i.e. where the short-wavelength disturbance breaks down first, *and* where the short-wave core displacement is maximal. One observes the initially symmetric pair, the internal deformations, an irregular pattern due to the tilting of vorticity and mixing, and the final 'skeleton' pair, which persists for a long time. In figure 25 the phases of the long- *and* short-wave instabilities are opposite to the ones in figure 24: the primary vortices move away from each other and the centres are displaced in opposite directions. As expected, the internal deformations develop more slowly, due to the lower mutually induced strain. The final image (figure 25f) shows that the regions where the dye

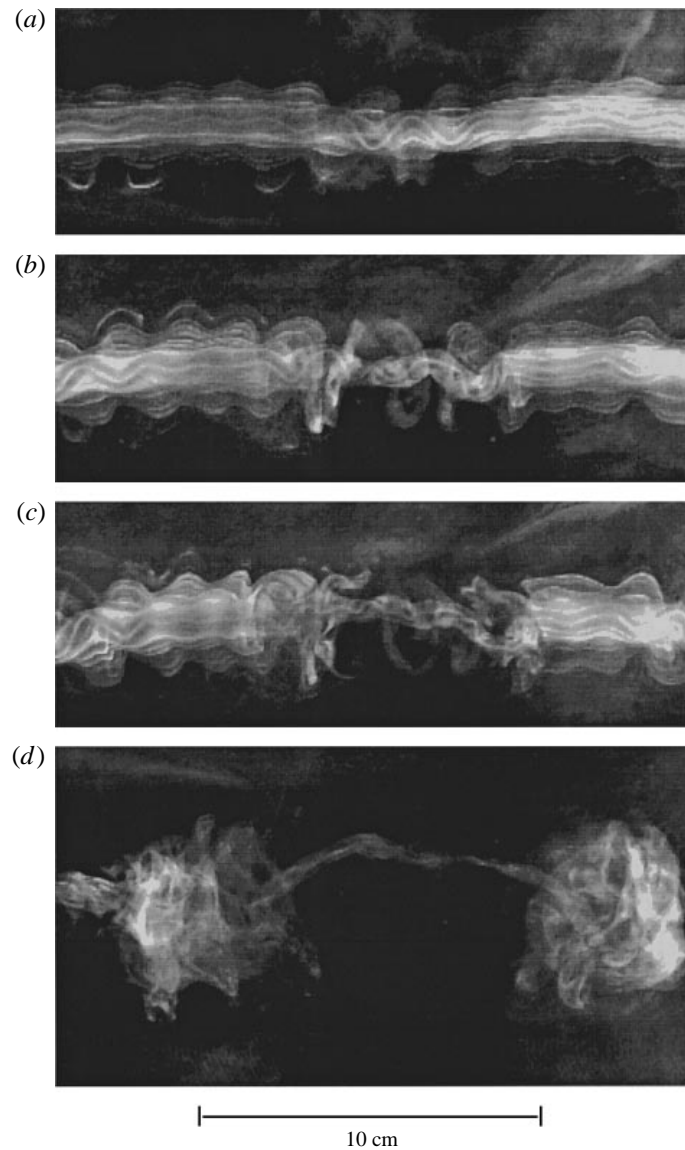


FIGURE 23. Visualization of the breakdown of the short-wavelength perturbation in side view (the pair moves down), where only the far vortex is dyed. $Re \approx 2700$. (a) $t^* = 7.2$, (b) $t^* = 8.6$, (c) $t^* = 9.4$, (d) $t^* = 11.2$. Images (a–c), show an area of approximately $6 \text{ cm} \times 18 \text{ cm}$, and the sequence covers a time of about 6 s in real time.

concentrates in figures 22 (c) and 23 (d) indeed do not contain large vigorous coherent structures anymore.

For each of these sequences, the evolution of the (average) circulation of the vortices was calculated by numerically performing line integrals around the vorticity distributions in figures 24 and 25. The result in figure 26 confirms the previous observations. In the plane where the vortices approach, the primary circulation starts to decrease first, at about the time when the pair begins to slow down at $t^* = 6$ (figure 18). After a transition period it reaches a value of about 30% of the initial

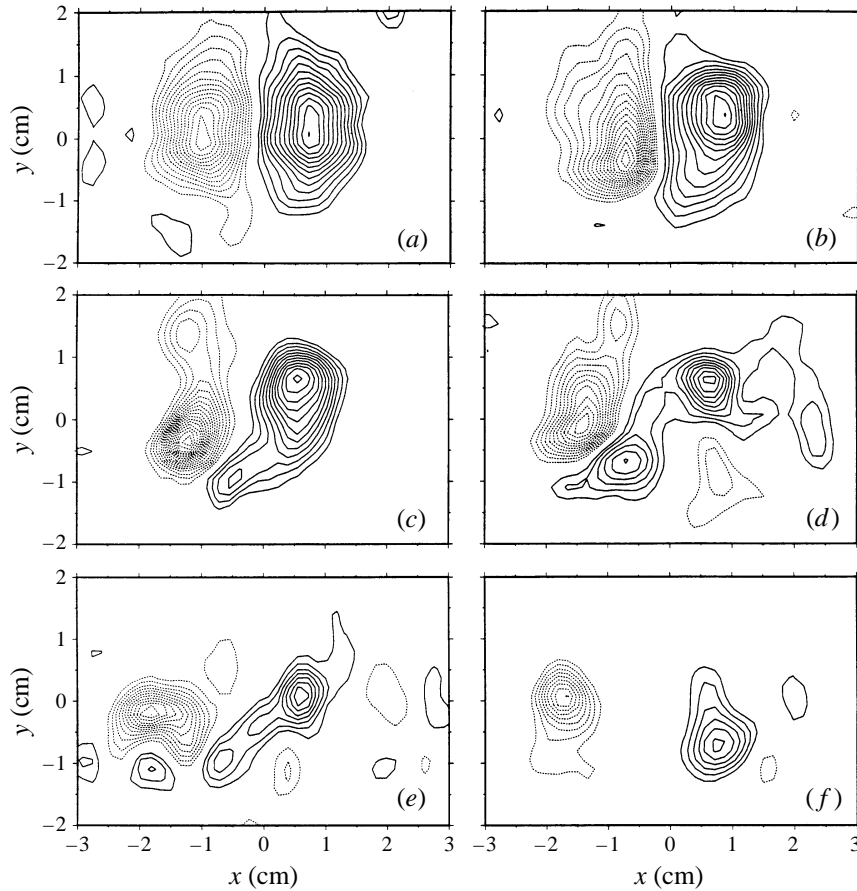


FIGURE 24. Contours of axial vorticity at a position where the large-scale instability brings the vortices closer together. $Re = 2660$. (a) $t^* = 5.4$, (b) $t^* = 7.1$, (c) $t^* = 8.4$, (d) $t^* = 9.4$, (e) $t^* = 10.1$, (f) $t^* = 12.5$. Contours are separated by $\Delta\omega_z = 0.86(\Gamma_o/2\pi b_o^2)$.

circulation. This represents the circulation of the final skeleton pair. (For comparison, the similar threads of vorticity linking the late-time vortex rings after reconnection, in the case of a pure Crow instability, have only about 10% of the initial circulation (Lewke & Williamson 1998 *a*.) The drop in circulation in the other plane commences after the case described above, but for large times it decreases to much lower values, confirming the absence of large coherent structures in the late stages of this flow.

6. Conclusions

In this study, we have obtained much new information about the short-wavelength instability of a freely developing counter-rotating vortex pair, through carefully controlled experiments. Extensive flow visualizations and quantitative velocity measurements with digital particle image velocimetry were used to reveal the complicated spatial structure of the disturbance associated with this instability.

The short-wavelength instability consists of an internal deformation of the vortex cores, involving a wavy displacement of the vortex centre, the existence of a cylindrical invariant stream tube, and a radial motion of fluid, which is in opposite directions

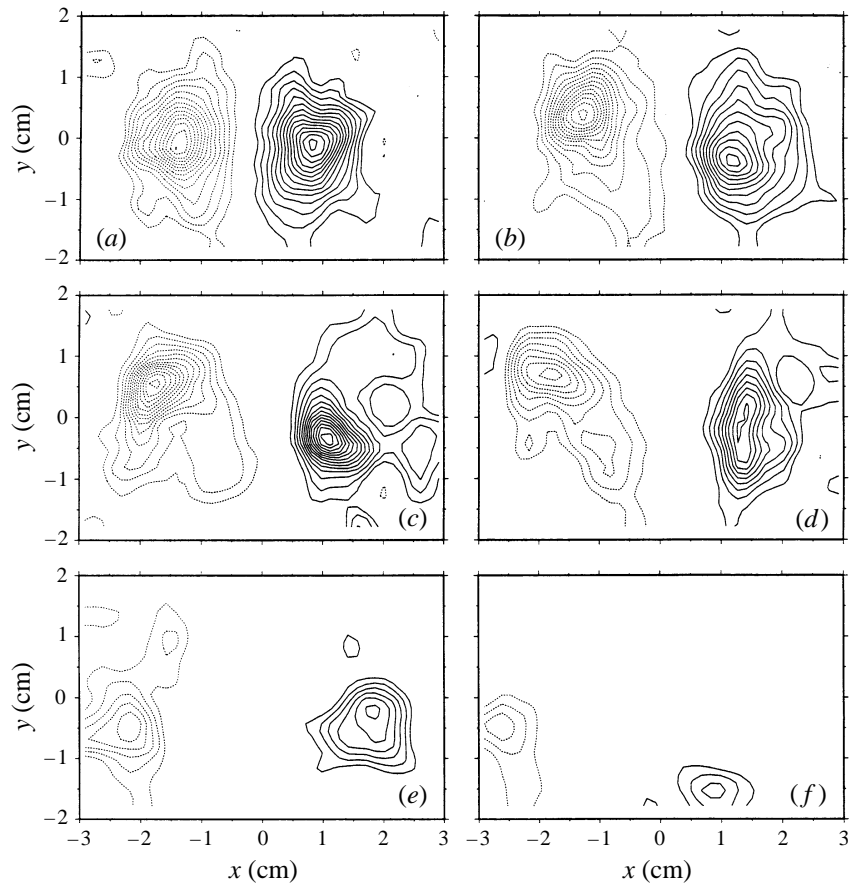


FIGURE 25. Contours of axial vorticity at a position where the large-scale instability separates the vortices. $Re = 2660$. (a) $t^* = 5.5$, (b) $t^* = 8.3$, (c) $t^* = 9.1$, (d) $t^* = 10.1$, (e) $t^* = 12.1$, (f) $t^* = 14.4$. Contour spacing as in figure 24.

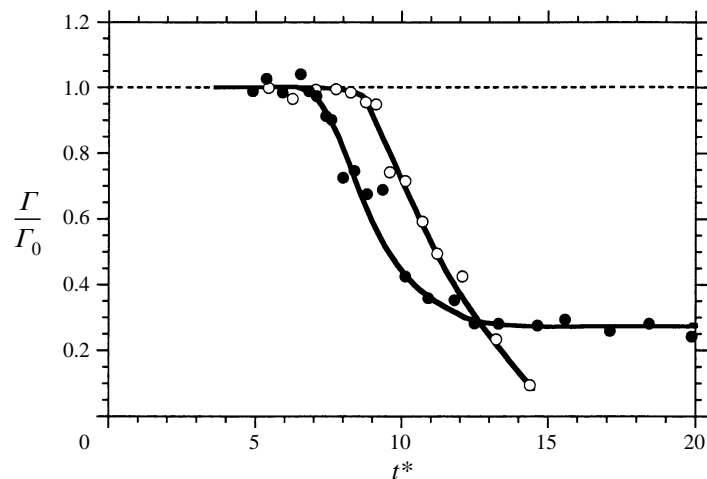


FIGURE 26. Evolution of the circulation in planes perpendicular to the initial vortex axes, measured with DPIV. Solid circles represent data measured in a plane where the large-scale (Crow) instability brings the vortices closer together, open symbols show data in planes where they are separated. $Re = 2660$.

inside and outside this tube. An analysis and comparison of different theories treating vortex pair instabilities and the dynamics of strained vortices have led us to identify this phenomenon as a manifestation of an elliptic instability of the vortex cores. The streamlines in the core of each vortex have an elliptical shape due to the interaction of the vorticity with the mutually induced strain, and this kind of flow is known to be receptive to three-dimensional instability. Qualitative and quantitative comparisons between our experimental observations, and predictions derived from the theory on elliptic instability show good agreement.

The scaling of the spatial instability characteristics on the vortex core size was determined from the experiments. It is found, for the vortex pair, that the invariant streamline is located at a radial distance from the vortex centre closely equal to the characteristic radius a of the Oseen model (2.1) representing real vortices. This is close to 90% of the radius of maximum circumferential velocity. The axial wavelength was found to be twice as large as the diameter of the invariant streamline, i.e. nearly equal to $4a$, again in agreement with the elliptic instability theory.

Not only the spatial features, but also the growth rate of the short-wave disturbance, which we were able to determine experimentally, compares well with theoretical predictions. The existence of short waves on strained vortices has been documented earlier for the cases of vortex rings (e.g. Krutzsch 1939 or Maxworthy 1972) and asymmetric vortex pairs (Thomas & Auerbach 1994). However, to our knowledge, this is the first time that the elliptic instability mechanism has been identified as the origin of these waves, and analysed in detail experimentally in a real open flow. The fact that the spatial and temporal characteristics in our finite, non-uniform elliptical flow are extremely similar to the theoretical results obtained for an infinite uniform flow (except, of course, for the selection of a discrete instead of a continuous set of instability modes), supports the suggestion that elliptic instability is a general mechanism for transition in a large class of strained vortical flows.

We discover that the instabilities of the two vortices evolve in a 'cooperative' manner, in that a distinct phase relationship is found between the perturbations on each vortex, which breaks the initial symmetry of the pair with respect to the central plane, and in which the displacements of the vortex centres are in the form of an antisymmetric mode. We explain this unexpected phenomenon, whereby the instabilities on each vortex are coupled, by considering that the antisymmetric mode is the only one which satisfies a kinematic matching condition between the two perturbations.

The long-term evolution of the instability is linked to the special geometry of the counter-rotating vortex pair flow. The growing initial deformations of the translating pair finally provoke a periodic cross-over of fluid from one side to the other, close to the front stagnation point. This results in an array of secondary vortex pairs, perpendicular to the primary vortices, that quickly lead to a destruction of the organized initial perturbation. The growth of these transverse secondary vortices and the breakdown are accompanied by a significant decrease of the primary vortex circulation and the self-induced descent speed of the pair, as well as a rapid energy transfer to even smaller scales. This behaviour is quite different from the case where the vortex pair experiences only the Crow instability, and where the developing large-scale vortex rings remain very energetic for long times. This modification of the decay scenario by the presence of the short-wave instability could have important implications on the study of trailing vortices in aircraft wakes.

Finally, the development of the short-wavelength instability and the late evolution of the flow were found to be strongly influenced by the long-wave Crow instability.

Since it induces a periodic change of the distance between the vortices, and therefore of the mutually induced strain, the growth of the elliptic instability is modulated on the same scale. The subsequent breakdown is also not uniform along the vortex axes, but sets in at periodic locations separated by one Crow wavelength. In the final stages of the flow development, the vortical fluid initially making up the pair is collected by strong axial motion into distinct periodic regions of unorganized turbulent motion. Apparently, the classical Crow instability, whereby distinct vortex rings evolve, is inhibited by the combined action of the short- and long-wavelength instabilities.

Complementary animations and extensive colour visualizations of both the short-wave instability investigated in the present work, and also the long-wavelength instability which is studied in Leweke & Williamson (1998 *a*), are included in an electronic paper (Leweke & Williamson 1998 *b*).

The authors wish to thank S. Le Dizès for helpful comments on the elliptic instability. The financial support from the Deutsche Forschungsgemeinschaft (Grant No. Le 972/1-1 (TL)), the US Office of Naval Research (Contract No. N00014-95-1-0332 (CHKW)), and NATO (Grant No. CRG 970259) is gratefully acknowledged.

REFERENCES

- ABRAHAMSON, S. & LONNES, S. 1995 Uncertainty in calculating vorticity from 2D velocity fields using circulation and least-squares approaches. *Exps. Fluids* **20**, 10.
- BAYLY, B. J. 1986 Three-dimensional instability of elliptical flow. *Phys. Rev. Lett.* **57**, 2160.
- BAYLY, B. J., HOLM, D. D. & LIFSCHITZ, A. 1996 Three-dimensional stability of elliptical vortex columns in external strain flows. *Phil. Trans. R. Soc. Lond. A* **354**, 895.
- CADOT, O., DOUADY, S. & COUDER, Y. 1995 Characterization of the low-pressure filaments in three-dimensional turbulent shear flow *Phys. Fluids* **7**, 630.
- CRAIK, A. D. D. & CRIMINALE, W. O. 1986 Evolution of wavelike disturbances in shear flows: a class of exact solutions of the Navier-Stokes equations. *Proc. R. Soc. Lond. A* **406**, 13.
- CROW, S. C. 1970 Stability theory for a pair of trailing vortices. *AIAA J.* **8**, 2172.
- DELISI, D. & ROBINS, R. 1997 Small-scale instability in trailing wake vortices in a stratified fluid. *AIAA Paper* 97-1784.
- DIDDEN, N. 1977 Untersuchung laminarer, instabiler Ringwirbel mittels Laser-Doppler-Anemometrie. *Mitt. aus dem MPI für Strömungsforschung und der AVA*, vol. 64. Göttingen, Germany.
- ELGOBASHI, S. 1994 On predicting particle-laden turbulent flows. *Appl. Sci. Res.* **52**, 309.
- ELOY, C. & LE DIZÈS, S. 1998 Instability of the Burgers and Lamb-Oseen vortices in a strain field. *J. Fluid Mech.* (submitted).
- GUEZENNEC, Y. G. & KIRITSIS, N. 1995 Statistical investigation of errors in particle image velocimetry. *Exps. Fluids* **10**, 138.
- KELVIN, LORD 1880 On the vibrations of a columnar vortex. *Phil. Mag.* (5) **10**, 155.
- KIDA, S. 1993 Tube-like structures in turbulence. *Lecture Notes Numer. Appl. Anal.* **12**, 137.
- KRUTZSCH, C.-H. 1939 Über eine experimentell beobachtete Erscheinung an Wirbelringen bei ihrer translatorischen Bewegung in wirklichen Flüssigkeiten. *Ann. Phys.* (5) **35**, 497.
- LANDMAN, M. J. & SAFFMAN, P. G. 1987 The three-dimensional instability of strained vortices in a viscous fluid. *Phys. Fluids* **30**, 2339.
- LEBLANC, S. & CAMBON, C. 1997 On the three-dimensional instabilities of plane flows subjected to Coriolis force. *Phys. Fluids* **9**, 1307.
- LEBLANC, S. & CAMBON, C. 1998 Effects of the Coriolis force on the stability of Stuart vortices. *J. Fluid Mech.* **356**, 353.
- LEWEKE, T. & WILLIAMSON, C. H. K. 1998 *a* Long-wavelength instability and reconnection of a vortex pair. *J. Fluid Mech.* (submitted).
- LEWEKE, T. & WILLIAMSON, C. H. K. 1998 *b* Visualization of vortex pair instabilities. *Intl J. Fluid Dyn.* (<http://www-ijfd.swan.ac.uk/>) (submitted).

- LIFSCHITZ, A. 1994 On the stability of certain motions of an ideal incompressible fluid. *Adv. Appl. Math.* **15**, 404.
- LIFSCHITZ, A. & HAMEIRI, E. 1991 Local stability conditions in fluid dynamics. *Phys. Fluids A* **3**, 2644.
- LOCKE, C. A., HIRSA, A. & RUBIN, M. D. 1993 Short-wave instability in a laminar vortex pair. In *ASME Fluids Engng Conf., Forum on Unsteady Flows* (ed. W. L. Keith & T. Wei). FED-Vol. 157, p. 73. ASME.
- MALKUS, W. V. R. 1989 An experimental study of global instabilities due to the tidal (elliptical) distortion of a rotating elastic cylinder. *Geophys. Astrophys. Fluid Dyn.* **48**, 123.
- MAXWORTHY, T. 1972 The structure and stability of vortex rings. *J. Fluid Mech.* **51**, 15.
- MOORE, D. W. & SAFFMAN, P. G. 1971 Structure of a line vortex in an imposed strain. In *Aircraft Wake Turbulence and its Detection* (ed. J. H. Olsen, A. Goldberg & M. Rogers), p. 339. Plenum.
- MOORE, D. W. & SAFFMAN, P. G. 1975 The instability of a straight vortex filament in a strain field. *Proc. R. Soc. Lond. A* **346**, 413.
- PIERREHUMBERT, R. T. 1986 Universal short-wave instability of two-dimensional eddies in an inviscid fluid. *Phys. Rev. Lett.* **57**, 2157.
- ROBINSON, A. C. & SAFFMAN, P. G. 1984 Three-dimensional stability of an elliptical vortex in a straining field. *J. Fluid Mech.* **142**, 451.
- SAFFMAN, P. G. 1992 *Vortex Dynamics*. Cambridge University Press.
- THOMAS, P. J. & AUERBACH, D. 1994 The observation of the simultaneous development of a long- and a short-wave instability mode on a vortex pair. *J. Fluid Mech.* **265**, 289.
- TSAI, C.-Y. & WIDNALL, S. E. 1976 The stability of short waves on a straight vortex filament in a weak externally imposed strain field. *J. Fluid Mech.* **73**, 721.
- VINCENT, A. & MENEGUZZI, M. 1991 The spatial structure and statistical properties of homogeneous turbulence. *J. Fluid Mech.* **225**, 1.
- VLADIMIROV, V. A., MAKARENKO, V. G. & TARASOV, V. F. 1987 Experimental investigation of non-axisymmetric inertia waves in a rotating fluid. *Fluid Dyn.* **22**, 151.
- WALEFFE, F. 1990 On the three-dimensional instability of strained vortices. *Phys. Fluids A* **2**, 76.
- WESTERWEEL, J. 1994 Efficient detection of bad vectors in particle image velocimetry. *Exp. Fluids* **16**, 236.
- WIDNALL, S. E., BLISS, D. B. & TSAI, C.-Y. 1974 The instability of short waves on a vortex ring. *J. Fluid Mech.* **66**, 33.
- WIDNALL, S. E., BLISS, D. B. & ZALAY, A. 1971 Theoretical and experimental study of the instability of a vortex pair. In *Aircraft Wake Turbulence and its Detection* (ed. J. H. Olsen, A. Goldberg & M. Rogers), p. 305. Plenum.
- WIDNALL, S. E. & SULLIVAN, J. P. 1973 On the stability of vortex rings. *Proc. R. Soc. Lond. A* **332**, 335.
- WILLERT, C. E. & GHARIB, M. 1994 Digital particle image velocimetry. *Exps. Fluids* **10**, 181.